The Genesis Solar Wind Concentrator

Jane E. Nordholt[1],
(correspondence author)
M/S D454
Los Alamos National Laboratory
Los Alamos, NM 87545
JNordholt@LANL.gov
505-667-3897

Roger C. Wiens[1], Rudy A. Abeyta[1], J. Roberto Baldonado[1], Donald S. Burnett[2], Patrick Casey[3], Daniel T. Everett[1], Joseph Kroesche[4], Walter Lockhart[5], Paul MacNeal[4], David J. McComas[3], Donald E. Mietz[1], Ronald W. Moses, Jr. [1], Marcia Neugebauer[6], Jane Poths[1], Daniel B. Reisenfeld[1], Steven A. Storms[1], Carlos Urdiales[3]

Submitted to

Space Science Reviews
As Part of the Special Section
on the Genesis Discovery Mission

December 15, 2001

Submitted in revised form, May 21, 2002

---

[1] Los Alamos National Laboratory, Los Alamos, NM
[2] California Institute of Technology, Pasadena, CA
[3] Southwest Research Institute, San Antonio, TX
[4] Mobius Systems, San Antonio, TX
[5] Creative Circuitry, San Antonio, TX
[6] Jet Propulsion Laboratory, Pasadena, CA

Abstract

The primary goal of the Genesis Mission is to collect solar wind ions and, from their analysis, establish key isotopic ratios that will help constrain models of solar nebula formation and evolution. The ratios of primary interest include $^{17}O/^{16}O$ and $^{18}O/^{16}O$ to ±0.1%, $^{15}N/^{14}N$ to ±1%, and the Li, Be, and B elemental and isotopic abundances. The required accuracies in N and O ratios cannot be achieved without concentrating the solar wind and implanting it into low-background target materials that are returned to Earth for analysis. The Genesis Concentrator is designed to concentrate the heavy ion flux from the solar wind by an average factor of at least 20 and implant it into a target of ultra-pure, well-characterized materials. High-transparency grids held at high voltages are used near the aperture to reject >90% of the protons, avoiding damage to the target. Another set of grids and applied voltages are used to accelerate and focus the remaining ions to implant into the target. The design uses an energy-independent parabolic ion mirror to focus ions onto a 6.2 cm diameter target of materials selected to contain levels of O and other elements of interest established and documented to be below 10% of the levels expected from the concentrated solar wind. To optimize the concentration of the ions, voltages are constantly adjusted based on real-time solar wind speed and temperature measurements from the Genesis ion monitor. Construction of the Concentrator required new developments in ion optics; materials; and instrument testing and handling.

1. Introduction

The goal of the Genesis mission is to determine the elemental and, in particular, the isotopic composition of the original solar nebula. Because the Sun contains more than 99.5% of the solar system mass and because the outer layers of the Sun are thought to be relatively unchanged in composition over time, the solar photospheric composition is essentially equivalent to the composition of the solar. While some fractionation (preferential ion selection processes) undoubtedly occurs in the formation and acceleration of the solar wind (Bochsler; 2000, Bodmer and Bochsler; 2000), we believe this can be modeled and constrained by the collection of different solar wind flow regimes (Burnett et al.; 2002) to an accuracy sufficient to place significant limits on the solar nebula constituents and evolution. A definitive measure of this composition would serve as a baseline for understanding differences in the present composition of solar system bodies. Key isotopic ratios include the $^{17}O/^{16}O$, $^{18}O/^{16}O$, $^{15}N/^{14}N$, $^{13}C/^{12}C$, and noble gas isotopic ratios. Other objectives include the Li/Be/B elemental and isotopic abundances, which should help constrain models of solar evolution, and the radioactive nuclei (^{14}C, ^{10}Be), which should constrain models of the recent solar-surface energetic particle flux. Oxygen isotopic heterogeneity among solar system bodies (e.g., Clayton; 1993), cannot be interpreted without putting it in the context of the solar oxygen isotopic composition (Wiens et al.; 1999). Likewise, the evolution of planetary atmospheres, particularly in terms of the change in ratio of ^{15}N to ^{14}N and the ratios of the noble gas isotopes, cannot be correctly modeled without knowledge of the primordial composition (cf. Pepin; 1991).

In-situ mass spectrometric analysis of the solar wind isotopic composition is hampered by the large range of charge states and energies within the solar wind and especially by the large required dynamic range (e.g. $^{17}O / ^{16}O \approx 4x10^{-4}$). While lower precision measurements of N (Kallenbach et al.; 1998), O (Harris et al.; 1987, Collier et al.; 1998, Wimmer-Schweingruber et al., 2001), Ne (Kallenbach et al., 1997), Si, Fe, Cr, and a few other isotopes have been made by in-situ mass spectrometers, the Genesis mission takes a different approach by collecting samples of the solar wind to return to Earth for analysis.

The idea of implanting solar wind ions in target materials that are returned to Earth has a long and distinguished heritage dating back to the first published analysis of the methodology (Bühler et al.; 1965). As part of many of the Apollo landings on the Moon, thin foils of Al or Pt were exposed to the solar wind on the lunar surface and returned to Earth (cf. Geiss et al.; 1969, Geiss et al.; 1970, Geiss et al.; 1972). These measurements are today still benchmarks of the noble gas isotopic composition of the solar wind. The technique of increasing solar wind fluence with electrostatic fields was also discussed by Signer (1965). The Concentrator builds on this concept to produce an electrostatically focused solar wind collector that uses ultra-pure targets for sample collection and return. The basic concentrator concept, as originally proposed for Genesis, is described by McComas et al. (1998).

The Genesis mission was launched in August 2001 and traveled to the L1 point between Earth and the Sun where it is exposing collector materials to the solar wind, a mission segment that will last over 2 years, and will then return the samples to Earth for ground-based analysis. After sample return in fall 2004, analyses of target materials will take place using a number of techniques. The isotopic abundances of the implanted solar wind in these samples and by proxy the solar composition will be determined to levels of accuracy required by planetary science applications.

The primary difficulty with the Genesis concept is the low fluence of ions heavier than helium in the solar wind. Measuring the isotopic abundances of some key elements such as O and N is difficult using simple passive collection. This is because large (>50 cm^2 areas) must be analyzed and because only one material (float zone Si) has adequate bulk purity. However, float zone Si has a native oxide layer and, because of SiN formation, extraction N from large areas of Si is difficult. Consequently, to optimize signal to background, allowing the determination of these isotopic ratios, the Genesis payload includes a large-aperture solar wind Concentrator designed to increase by an average factor of ~20 the fluence of isotopes in the m/q range of 2.0 to 3.6 amu/charge (essentially masses 4 to 28). The Concentrator also increases the average energy of ions entering the target, implanting solar wind ions below the native oxide layer. Table I lists estimated elemental abundances normally seen in the solar wind and their expected implantation levels in the Concentrator targets.

2. Overview

The Genesis spacecraft is designed to orbit the L1 point between the Earth and the Sun for nearly 28 months while collecting solar wind. It is pointed into the solar wind

4.5±2.0° off a direct line of sight to the Sun such that it will be directly facing the apparent average solar wind direction. The spacecraft will then return to Earth and its sample return capsule will parachute back to Earth where the samples that have been implanted with solar wind will be removed and distributed to laboratories for elemental and isotopic analysis.

The Genesis Concentrator is a unique instrument in that it does not send back any data from space other than simple state-of-health housekeeping data. Instead, its targets will be removed for analysis at the end of the mission. Figure 1 shows the Concentrator inside the spacecraft's science canister which prevents contamination during the launch, flight, and re-entry phases of the mission. Once on station at L1 the science canister is opened as shown to expose the Concentrator to the solar wind.

The Concentrator includes many novel developments: a new design for electrostatic mirrors; new testing methodologies; ultra-clean shipping and handling in the final stage of flight preparation; ultra-fine, ultra-strong stainless steel mesh; O-free resistive coatings for ceramic components; and high precision segments of ultra pure SiC, ^{13}C enhanced CVD diamond, and low N amorphous diamond film on a Si substrate (Jurewicz et al., 2002).

2.1 Operation

Figures 2 and 3 show the Concentrator's final design in partially cut-away cross-section and cut-away 3-dimensional views. Ions from the solar wind come from the upper portion of these figures, the direction pointed into the solar wind in the operational configuration. Ions initially traverse the first, grounded grid to enter the Concentrator. The outermost grid and instrument skin must be at spacecraft ground to prevent stray electric fields from the Concentrator from interfering with other parts of the spacecraft. The next grid down is the hydrogen-rejection grid. This grid is biased such that at least 90% of the solar wind protons are rejected in order to minimize proton radiation damage to the target. Rejection of this fraction of solar wind protons without also rejecting heavy ions requires that the hydrogen rejection grid voltage maintains a constant ratio relative to the peak of the solar wind proton energy distribution. The Genesis ion monitor (Barraclough et al., 2002), together with the science algorithm (Neugebauer et al., 2002) provide the energy levels every 2.5 minutes to update rejection grid voltages. The upper two panels in Figure 4 show how variations in the voltage on the hydrogen-rejection grid change the amounts of hydrogen and heavy ions rejected vs. electrostatic ratio of voltage to the peak of the solar wind proton energy distribution. The voltage on the hydrogen-rejection grid is $V_H = Ep * R$ where Ep is a running average of three measurements of the peak of the proton energy distribution from the ion monitor (Barraclough et al., 2002), and R is the ratio. The lower panel of Figure 4 shows the fractionation, or change in the isotopic ratios due to the Concentrator, of oxygen as a function of ratio R and thermal Mach number. The losses and fractionation limit the voltage level at which the hydrogen-rejection grid can be operated and still achieve the desired collection of heavy ions. A thorough analysis of the mass fractionation in the Concentrator is presented in Wiens et al., (2002).

Ions which successfully transit the hydrogen-rejection grid, will next have their group velocity, the velocity of energy propagation, increased relative to its value in the solar wind while their relative angular scattering is decreased as they approach the "acceleration" grid. The acceleration energy acquired by ions as they approach the acceleration grid is $E_a = - qV_a$ where q is the ion's charge and V_a is the voltage applied to the acceleration grid. The total energy of an ion is $E_t = - qV_a + E_i$ after it passes through the acceleration grid, where E_i is the ion's original energy in the solar wind. The acceleration accomplishes two goals: 1) it straightens the ion trajectories, allowing higher concentration factors, and 2) it provides higher energy implantation into the target. The acceleration voltage will be fixed at -6.5kV during operation and –10kV is the maximum allowed in the design. After passing through the acceleration grid, ions enter the field-free acceleration "can," a region in which all ions maintain their trajectories and energies of $- qV_a + E_i$. Having passed through the acceleration can, the ion must then pass through the "domed" or mirror grid which is part of the acceleration can and is maintained at the same voltage as the acceleration grid. The acceleration can is clearly visible in Figures 2 and 3 and is made up of the acceleration grid, the domed grid, and the outer can wall shown in green in Figure 2. Ions are reflected in the region between the domed grid and the bottom "mirror" electrode which is maintained at a positive voltage of up to +10kV. The region between the mirror grid and the mirror electrode forms a "mirror field" which acts to reflect ions and focus them onto the target. Like the hydrogen rejection grid, the mirror electrode voltages are adjusted in real time based on monitor and science algorithm data. The voltage on the mirror electrode is set to give a 20% margin in energy on the highest expected oxygen m/q, of 3.6, based on $^{18}O^{+5}$, therefore the mirror voltage is $V_m = 4.32*Ep$ and will produce a mirror point in most ion's trajectories well away from the mirror electrode. Ion trajectory turn-around far from the mirror is necessary because the mirror electrode itself is not a smooth surface. It has been microstepped as shown in Figure 5 so that optically it appears to be a flat plate reflecting the Sun's photons back to space but the electric field it produces at a distance several times the height of the microsteps (100µm) will smoothly focus the solar wind ions. Microstepping is a necessity if the target temperature is to be below ~250ºC to prevent implanted ions from being boiled off. Testing showed that less than one percent of the total incident optical flux was focused onto the target region by the mirror electrode. Ions reflected by the mirror field travel back into the acceleration can transiting the domed grid once again. Having re-entered the acceleration can the ions again have the total energy E_t described above. Ions are now focused onto the target area in which they are then implanted at a depth which has been increased by the additional acceleration component, $-qV_a$, of their total energy. The target's sensitive area, which faces downward in Figures 2 and 3, is made up of SiC, amorphous diamond film on a Si substrate, and ^{13}C enhanced CVD diamond sections (Burnett et al. 2002) which are clearly visible in Figure 6.

2.2 Mechanical/Cleanliness Requirements

The grids that carry the Concentrator's operating voltages and form the desired electric fields must have as high an open area ratio as possible while still maintaining structural integrity and highly uniform electric fields. A grid pitch of at least 20 lines/cm (50 lines/inch or lpi) is necessary to maintain field uniformity. However, because ions must pass through 5 grids (twice through the domed grid) to reach the target, all grids must have open area ratios A ≥ 0.90 because the percentage of ions that transit all grids is geometrically A^5. Thus the grid wires can have a maximum thickness in the direction parallel to the surface of the grid of ≤26μm. The grids used in the Concentrator are woven from 25μm stainless steel wires on a 50 lpi pitch which gives them an open area ratio 90.4%. All structures supporting the grids and elsewhere in the Concentrator flight region were likewise minimized to prevent the loss of ions from collisions with these structures. Although grid support frames are only a few millimeters thick these structures also can perturb the desired electric fields and were placed on the side of the grids that minimized the field variations they cause. For the grounded grid the structure is above the grid in the low field region around the spacecraft. The hydrogen-rejection grid has, on average, a lower field strength on the side closer to the grounded grid, therefore the structure supporting the hydrogen-rejection grid is on the side nearest to the grounded grid. The volume inside the acceleration can is a field-free region therefore the acceleration grid's supporting structure is below its grid and the support for the domed grid is above its grid.

The ultra-clean requirements mean that the electronics must be sealed away from the Concentrator and the internal portion of the sample-return canister. The electronics boxes were therefore mounted on the bottom side of the Concentrator's base plate. The base plate forms a seal with the sample-return canister's deck using a low vapor pressure o-ring. All electronics connections are made through hermetic feed-throughs welded into the Concentrator's base plate and all of the feed-through parts and wiring for the high voltages on the clean side of the Concentrator base plate are ultra-low outgassing ceramic or metal components. By using the hermetic seal, standard flight electronics could be used without causing contamination to the Concentrator or any other collection materials mounted inside the sample-return canister. Voltages are input to each electro-optical component on hard connections which are wired to each of the feed-throughs with soldered connections to small wire jumpers. The solder was allowed despite cleanliness requirements because a low outgassing solder was used and, as is visible in Figure 3, the high voltage input section is largely sealed off from the rest of the Concentrator. Connections between the high voltage bus bars, small wire jumpers, and high voltage feed-throughs can be seen in Figure 3.

2.3 Testing

The Concentrator was subjected to all of the standard tests required of a flight instrument as well as being subjected to a unique characterization regimen designed to provide flight performance verification. After initial tests of a prototype confirmed that the Concentrator design would meet the scientific requirements, two Engineering Models (EMs) were constructed. Two EMs were required to meet the demanding integration and test schedule. One model was used for detailed thermal testing, including solar thermal vacuum grid mapping of the Concentrator alone (instrument level), and solar thermal vacuum testing of the Concentrator while integrated into the spacecraft canister as shown in Figure 1 (canister level). The use of two EMs allowed modification of the thermal EM for installation of thermocouples and associated wiring into the interior portions, including the target and grid frames. The flight model (FM) was tested at instrument and canister levels prior to final cleaning and gold coating, though as such it had to forego accurate thermal testing. This was acceptable because of the high fidelity of the EMs. After re-assembly, the FM was never exposed outside a clean room or clean vacuum chamber. This necessitated the unusual omission of a final workmanship vibration, but all of the final assembly techniques had been tested and verified several times on the EMs and were both performed and observed by multiple quality assurance personnel. Its flight-readiness was verified by high voltage testing to 105% of maximum operating voltages and a thorough final optical mapping which can be done under clean conditions and is described below.

3. Design and Development

The design goals of a concentration factor of at least 20 with a mass fractionation averaged across the target quantified to better than 0.1% was set to allow sufficiently detailed analysis of implanted material to provide the solar isotopic ratios of the $^{17}O/^{16}O$ and $^{18}O/^{16}O$ to +/-0.1%, and $^{15}N/^{14}N$ to +/-1% using the best analytic techniques available. These design requirements were primarily developed by comparing what could be collected from the solar wind in a reasonable mission length with the minimum content of O and N in ultra-pure materials and determining what would be required to analyze implanted O and N accurately. Besides concentration, the Concentrator must not introduce unknown levels of mass fractionation or fractionation gradients in the target that would inhibit the accurate analysis of the target. Table II shows the full list of performance criteria that were used throughout the development of the Concentrator. A numerical limit was not placed on the fractionation gradient but it has been checked to be small enough that it does not cause target samples to be analyzed in unworkably small radial segments (Wiens; 2002).

3.1 Mirror Design

Many different electro-optical configurations were tested but the most efficient is the ion analog of the optical reflecting telescope described above. This is because like an optical telescope, an ion telescope concentrates the flux which impinges on its aperture by using a large collection area well-focused onto a relatively small target. Designs which use multiple targets and apertures or electro-optical lenses to focus ions onto target areas were examined but ultimately the best concentration is achieved just as it is in telescopes—a large-area aperture, most compactly and cheaply produced with a mirrored configuration, is focused with high f-number optics onto a small target. The 6.2cm diameter of the Concentrator's target comes directly from the focusing ability of the ion mirror given the known angular and energy distributions of the solar wind. However, unlike with photon-optics, ion-optical mirrors that give high f-number focusing cannot be made achromatic with simple parabolic optics. The equivalent of photon-chromatic effects in ion optics is differential focusing which is energy-dependent. This is a major concern for the Concentrator because the solar wind accelerates all of its components to the same velocity and this means that any mass difference in component ions translates to an energy difference. Energy-dependent focusing is thus equivalent to mass fractionation which is unacceptable for the scientific investigation to be performed by the Concentrator.

This was corrected by developing an electro-optical design which produced a virtual parabolic surface at which the ions were reflected. The upper portion of Figure 7 shows the energy-dependent or chromatic focus of a design where similar parabolic mirror grid and electrode designs are used. No design of this type with similar parabolic electro-optical mirror elements will focus without chromatic distortions because the penetration of the ions into the mirror-field region varies with the angle between the mirror surfaces and the incident ion's direction. Ions of equal energy will penetrate less deeply into the mirror region at the edges of the mirror because the reflection point is determined by the component of particle's velocity which is parallel to the field lines. Thus ions in the more steeply inclined portion of the mirror near the edges turn around closer to the mirror grid than those in the central portion. As Figure 7 shows, this effect varies with ion energy and thus cannot be corrected by a simple adjustment of the focal length of the parabola. The lower half of Figure 7 shows the achromatic design developed for the Concentrator. In this design the loci of reflection points is parabolic and the surfaces of the mirror grid and mirror electrode diverge toward the edges of the Concentrator. This reduces the electric field in this region and compensates for the reduced velocity component parallel to the field lines.

3.2 The Hydrogen-Rejection and Acceleration Grids

While energy-dependent focusing has been eliminated from the ion mirror, there are still energy dependent effects associated with the hydrogen-rejection grid and the acceleration can. Since the voltages of both of these electro-optical components operate directly on only one component of an ion's velocity vector, they alter the trajectories of incoming ions. This energy-dependent effect cannot be corrected by adjusting the electric fields around the grids in the way that is done for the mirror, and constitutes the bulk of the remaining mass fractionation in the Concentrator. This problem is further compounded by the multiple charge states present in the solar wind and the fact that forces on the ion are proportional to an ion's charge multiplied by the grid voltage. Table III gives a sampling of the charge states for some isotopes found in the solar wind and their mass per charge ratios.

Figure 8 gives a schematic overview of the effects of the acceleration grid on the ion distribution hitting the target. The effect of the acceleration voltage is to narrow the angular distribution of ions with lower m/q more than the angular distributions of ions with higher m/q. This causes ions with lower m/q to be implanted more centrally in the target than ions with higher m/q. The hydrogen rejection grid acts to widen the angular distribution for ions with lower m/q more than for ions of higher m/q. The effects of the angular distribution changes introduced by the hydrogen rejection and acceleration voltages are not mutually cancelled out. Figure 9 shows the effect of different acceleration voltages on mass fractionation across the target. The planned operational acceleration voltage has been reduced from -10kV in the original flight plan to -6.5kV to reduce this effect. The final operational setting for the acceleration voltage was the result of a trade study in which the advantage of a lower mass fractionation gradient across the target is traded against a slightly higher concentration factor, lowered ion backscattering losses at the target surface, and deeper implantation depths. Mass fractionation resulting from the hydrogen-rejection grid is less easily reduced. Figure 4 shows the levels at which its voltage must be operated to reject the required 90% of the incoming hydrogen. This criterion cannot be relaxed without potentially damaging the target. The added mass fractionation that different levels of hydrogen-rejection grid voltages produce is discussed in detail in a companion paper to this one (Wiens et al., 2002). Table IV gives the parameters that will be used to set the voltage on the hydrogen rejection grid.

3.3 Operating Temperature

After the electro-optical design was complete, the Concentrator development team had to determine what temperature control measures were needed and how best to implement them in an ultra-clean instrument. The requirement that the Concentrator not introduce additional oxygen or nitrogen into the target from sputtered ions meant that the instrument's internal surfaces had to be coated with a material that would not form a native oxide layer or introduce N-bearing compounds. Gold is the most easily obtainable coating that meets these criteria. Unfortunately gold has a thermal absorption to emission (alpha / epsilon) ratio, which causes it to heat to an unacceptably high temperature in some parts of the Concentrator. A careful examination of other materials which are N-free and do not form native oxide layers established that they all had similar alpha to epsilon ratios. Active cooling could not be provided without violating the cleanliness requirements of the Concentrator (e.g. a micro-meteoroid-induced pinhole in a heat pipe would introduce contamination from coolant leakage) so other temperature mitigation methods had to be applied. The components of the Concentrator which have critical temperature control requirements are the target, the Concentrator Electronics Boxes (CEBs), and the grids. The most important element for which the operating temperature must be controlled is the target. The maximum target temperature above which diffusion would likely cause loss of the solar wind sample is 250°C. Microstepping the mirror electrode and placing the target behind an anodized sunshade (anodized materials have low alpha/epsilon ratios) reduced its operating temperature to an acceptable 230ºC, as a worst case calculation. The anodized coating on the sunshade is acceptable because it is external to the Concentrator's focusing elements and their structures. The CEBs are mounted on the anti-solar side of the sample-return canister and, with sufficient thermal control of the Concentrator's mounting plate, can be kept below an acceptable maximum operating temperature of 77ºC. Temperatures measured in the solar thermal tests performed on one of the Concentrator EMs are given in Table V.

Thermal measurements and control of the grids and their supports presented several different challenges. The mirror electrode and grid support frames were mounted in a self-centering fashion on a series of pins in radial grooves that allowed them to expand relative to the Concentrator's outer can which is cooled by radiation and by connection to the Concentrator's baseplate. The baseplate is then in contact with the temperature controlled sample-return canister deck. The grids were produced from the same type of stainless steel as the frames but the inability of the tiny wires that make up the grids (φ = 25μm) to efficiently radiate their heat to space in comparison to the larger frame members means that the grids are substantially warmer when in sunlight. This raises concerns about grid wrinkling and deflection by the electrostatic forces on them from their high voltages. Further, when the spacecraft is turned so that the Concentrator moves from sunlight to shadow, the fine grid wires, lacking thermal mass, cool immediately while the frames do not. This means the grids wrinkle in the sun and are severely stressed when moved into shadow. Grids need to be strong and very firmly attached to their frames without forcing the frame size to be large thereby blocking ions. Preliminary tests of grids mounted on hoops showed that woven mesh was far stronger than etched mesh. The Concentrator prototype used hexagonal 24 lines/cm (60 lpi) etched mesh for the flat grids and woven for the domed grid but all later Concentrators (both EMs and the FM) used woven mesh for all grids. Attachment of the grid to their frames was shown to be sufficiently strong both for grids spot welded to their frames with a cover-shim or for grids clamped to their frames in concentric hoop mounts. For grids in areas critical for ion blockage, the hydrogen-rejection and acceleration grids, grids were spot welded to minimize frame size. Grids that had less critical areal constraints and were subject to more risks from handling, the ground and acceleration grids, were hoop mounted. The domed grid and grounded grid were both hoop mounted while the acceleration and hydrogen-rejection grids were spot welded. In both cases grids were bonded to only the inner and outer rings, and not to the radial ribs, to allow for greater flexibility of the mesh during heating or cooling events. Tests with grids in a solar thermal vacuum chamber demonstrated that rigidly mounted woven mesh could withstand the stresses induced by the thermal shock which occurs when the Concentrator is moved from full sunlight to shade, however the high operating temperature of the grids in comparison to that of their frames and the consequent wrinkling and sagging of the grids was unacceptable if the grids were gold coated. Careful analysis of the likelihood of material sputtering off uncoated grids and implanting in the target showed that, largely because of the very high open area of the grids, they could be left uncoated. The increased thermal emission of bare stainless steel relative to gold surfaces keeps the grids at a much lower temperature and does not cause significant wrinkling or sagging when in full sunlight.

3.4 Domed Grid

Another major concern was the structural integrity of the domed grid. The waffle-patterned support shown in Figure 3 was found to be optimal for strength with minimal ion blockage however when grid was mounted on this frame using a mandrel to produce a grid surface with the correct curvature, the grid was able to move and change its figure. There were concerns about how best to test the Concentrator mimicking the zero gravity and electrostatic forces on them. SIMION modeling showed that some defocusing caused by stretching the grid tightly over its frame, in fact, reduces mass fractionation and the fractionation gradient in the Concentrator target (Wiens et al.;2002). The second engineering model and the flight model used grids stretched tightly over the domed grid frame. This configuration has very good structural stability under all of the conditions in which the Concentrator must operate. As shown in Figure 10, support structures and grids were included in SIMION models. Also an analytic function for scattering by the grids was developed and integrated into the SIMION models showing that the 20 lines/cm (50 lpi) grids and their supports did not unduly change the ion focusing of the Concentrator.

3.5 Flat Grids

The electrostatic forces on the grids were also examined. Although this is not an issue for the tightly stretched domed grid, the flat grids have long unsupported spans that help them to withstand the sudden temperature changes that occur when the spacecraft moves off sun pointing or covers the Concentrator with the collection arrays. The electrostatic forces on these grids are between 0.005 and 0.031 N (away from the mirror electrode for the acceleration grid and toward the mirror electrode for the hydrogen-rejection and grounded grids), while gravity on Earth exerts ~0.018 N on the grids. Functional testing of the Concentrator in a vertical position such as that shown in Figure 11 where the gravitational forces are orthogonal to the electrostatic forces indicated that the grids could maintain their shapes adequately when these forces are applied.

3.6 High Voltage Power Supplies

The programmable voltages that run the Concentrator are produced by two Concentrator Electronics Boxes. Each CEB produces all 3 voltages needed to run the Concentrator (hydrogen rejection, accelerator, and mirror electrode voltages) and each voltage is individually controllable. Table VI lists all of the voltages needed in the Concentrator. Two CEBs are used to provide operational redundancy, which is further enhanced by separately wiring each CEB output voltage into the Concentrator. Each voltage is output onto a coaxial cable and input to the Concentrator through hermetic feed-throughs welded into the Concentrator base plate. The Concentrator is normally powered by CEB-1. In the event of any voltage failure, that CEB will be turned off and all voltages supplied by CEB-2. Because of the commanding scheme used, the two CEBs cannot be on at the same time but this is not prohibited by the high-voltage wiring configuration. Figure 3 shows the cabling, feed-throughs (produced by Reynolds Inc.), and high voltage input section. The jumper wires that join the connections from each CEB to the bus bar that distributes the voltage to the related electrostatic element are also clearly visible. The currents drawn are very modest, coming from two sources: 1) Photoelectrons produced at the ground and acceleration grids each contribute approximately –500 nA to the H rejection grid, and the mirror grid produces about –360 nA which is collected on the mirror electrode. 2) Resistive coatings on the insulators that hold the mirror electrode in place and support the target below the sunshade. These coatings, which are described more completely below, act as high value resistors connected to the mirror electrode, hydrogen rejection grid, and accelerator grid, drawing approximately 0.25 μA, 0.5nA, and 0.5 nA respectively. The CEBs are able to supply approximately 3 μA at each voltage, well above requirements. The CEBs underwent thermal vacuum tests at both the EM and FM levels by themselves to avoid contaminating the sensor head.

4. Testing and Characterization

The Concentrator has a unique design with a wide variety of requirements (see Table II) which are of primary importance to the scientific goals of the Genesis mission. As such 4 Concentrators (1 prototype, 2 EMs, and 1 FM) were built and subjected to a wide variety of tests. In addition to standard vibration, thermal vacuum (instrument mounted in vacuum with temperature variations on the mounting surfaces to determine overall operational temperature range), solar thermal vacuum (instrument mounted in vacuum and exposed to a solar optical source to determine operating conditions in space), and thermal cycling, numerous tests were developed specifically for the Concentrator.

The Concentrator is designed to collect solar wind ions using voltage levels calculated from solar wind speed derived from the onboard solar wind ion monitor data (Neugebauer et al. 2002, Barraclough et al. 2002). Its actual data will be collected by analyzing ions implanted in its target well after the mission is completed. Only a very limited number of flight-like targets could be analyzed to test the Concentrator's operation. Therefore in order to fully test and characterize the Concentrator it was necessary to develop several new methods of analyzing the implantation efficiency into the Concentrator's target and the overall operability of a Concentrator. For these purposes 4 methods of testing and verifying Concentrator operation were developed: micro-channel plate detector (MCP) testing; foil implantation; grid and surface mapping; and target implantation.

4.1 MCP Testing

The first method, shown in Figures 11 and 12, replaces the target with a set of MCPs and was developed to allow comparison of simulated performance with actual performance. The upper 3 grids of the Concentrator must be replaced with grids on frames specially designed to hold the MCP assembly but the field and grid configuration are identical to that used for flight. Using an imaging anode from Surface Science Inc., behind 3 MCPs, images of ions impinging in the target area of the Concentrator can be viewed in real time. Figure 11 shows a Concentrator EM with the MCP imaging assembly in place in the ion beam test facility. Figure 13 shows a typical beam spot as imaged by the MCPs both as the ions enter the test chamber and as they impact the target surface. Spot position comparisons with simulations were made by finding the two-dimensional Gaussian center of each recorded spot and the position of maximum count value in each spot and comparing them with the spot center calculated by SIMION. Figure 14 shows a comparison between MCP image spot maximum and gaussian center fit locations and SIMION calculations.

4.2 Foil Implantation Tests

Mechanical requirements prevented the MCP imaging area from reaching the edge of the target which prevented the MCP imaging method from verifying the Concentrator's operation near the edge of its target and by analogy, the outer portion of its aperture. The outer portion of the Concentrator aperture comprises a major portion of the overall aperture area and also suffers from field variations due to edge effects. The standard methods of eliminating edge effects would require relatively large gaps between the external housing and the grids and other electro-optical elements. This would be an inefficient use of the limited volume and footprint available to the Concentrator onboard the spacecraft. For these areas foil implantation can be used to check the results of simulations in the outer region of the target. The number of data points is small in comparison to that available from MCP testing and this method also requires an understanding of the full implantation and concentration operation including focusing efficiency and backscattering off the target. Foil implantation testing was performed by covering the target area with cleaned aluminum foil which has a very low background content of noble gases. The Concentrator was then exposed to beams of the noble gases He^+, Ne^+, and Ar^+ and the analysis of the implanted noble gases were then compared with the amount expected from implantation time and measurements of the beam made with a Faraday cup and a non-concentrated control sample implanted into another foil. These tests showed good agreement with predictions. Table VII shows a comparison of predictions from the simulations and measurement of implantation in the foils for one implantation test. This demonstrates both a good understanding and agreement with simulation of the Concentrator's optics, mechanical construction, and implantation processes.

4.3 Grid and Surface Mapping

Several times in the Concentrator's development and preparation for flight, its targets cannot be examined directly to verify its continued correct operation. Concentrator operation must also be verified without access to its target in thermal vacuum and solar thermal vacuum testing as well as after final flight cleaning and preparation. The MCPs and foil implantation cannot be used during thermal vacuum tests because the vacuum levels in these chambers are not sufficient. Also, when the Concentrator is finally assembled for flight, the targets in the Concentrator cannot be installed without partial disassembly of the upper portion of the flight instrument. Any misalignment, wrinkling, or damage to grids could be detrimental to the Concentrator's operation and must be detected before flight. After final flight assembly the Concentrator is put in a high vacuum chamber and brought to full voltage to verify that no loose wires have been included and the operation of the power supplies is checked in high vacuum where the self-tests and current monitors for each of the high voltages produced by the flight CEBs can easily be verified. However the Concentrator could not be exposed to any ion beams or other sources that may cause unintentional implantation in the targets. Nevertheless, the FM Concentrator must be verified to be within the performance specifications listed above in a way that does not expose it to any possible contamination or implantation. Since the detailed operation of the Concentrator depends most directly on the exact nature of the surfaces of each of the grids and the mirror electrode, operational factors can be determined by accurately mapping each of the electro-optical surfaces in a Concentrator. Thus a non-invasive method of analyzing the state of the Concentrator's electro-optical surfaces was needed. Laser mapping of the grid, support, and mirror surfaces together with raytracing of the ion optics made it possible to assess the state of the Concentrator without activating it. However, mapping the surfaces of grids which are more than 90% transmissive in a fully assembled instrument where most surfaces are not directly accessible, required the development of a unique optical mapping facility. Finely focused optical triangulation micrometers built by Precimeter proved capable of locating and determining the distance to a grid wire to within 0.1 mm and to 0.03 mm for solid surfaces. Each electro-optical surface of the Concentrator can be mapped for shape and alignment within tolerances on a 1mm by 1mm square grid using these sensors. A mapping facility using a 3-axis optical translation table to automatically raster the optical micrometer over the Concentrator and record the absolute position of each surface was developed. Figure 15 shows a schematic diagram of the laser micrometer's operation in the mapping system. The different focal ranges of a variety of these optical micrometers is coupled with the approximate distance the translation stages are programmed to maintain from the Concentrator so that each surface being mapped is differentiated from the other surfaces for each raster pass. A specification of no more than +/-3mm deviation from the ideal surface figure and no more than 0.3° misalignment with the housing was established using SIMION raytracing. A Concentrator meeting these surface requirements will electro-optically perform within design requirements.

Every effort was made to map Concentrators under all of the various conditions to which they are subject to understand any changes in surfaces that would occur from such environmental factors as heating or vibration. Maps from before and after vibration are shown in Figure 16 and illustrate the excellent dimensional stability of all Concentrator components. Although no micro-meteorite impact tests were performed on a Concentrator, the extremely strong woven grids are difficult to damage relative to other grids of the same open area ratio and do not fail catastrophically when cut because of the energy absorption afforded by the bending of the wires in the weave. Although micrometeoroid impact testing was not performed, the grids are expected to survive such impacts better than other mesh because a single wire can be broken without moving relative to its nearest neighbors or causing the grid to tear.

In addition to performing these critical verifications, the mapping facility was used to measure the added wrinkling expected in the grids when in space. When fully exposed to the Sun, as they will be throughout the collection portion of the mission, the grids wires are expected to be warmer than their support structures. Because of the extremely small diameter of the grid wires, their temperatures cannot be measured with any standard contact thermometer. The extremely rapid cooling of the grid wires when shadowed, requires that the state of the grids be measured while under direct insolation, making infrared temperature measurements very difficult. The mapping facility once again served to provide data on the actual state of the grids. The optical micrometers have a notch filter that allows them to operate in sunlight. The wrinkling of the grids under direct sunlight was measured in the LANL solar thermal vacuum test chamber by a straight-forward modification of the mapping facility which allowed it to map the grids through the chamber window. The measured wrinkling of the grids not only verified acceptable performance of the Concentrator under flight-like conditions but can also be used to estimate the temperature of the grids.

4.4 Instrument Modeling

Actual concentration factors and fractionation depend strongly on the actual solar wind conditions, which differ significantly from what could be achieved in the simulation chamber. Realistic solar-wind performance of the concentrator could only be modeled rather than duplicated in the lab. Modeling of the concentrator performance under actual solar wind conditions was carried out using a SIMION model as described in Wiens et al. (2002). The validity of the SIMION model was determined with data from the prototype, EM, and FM Concentrators by comparing simulations using the laser mapping data with the results of the MCP tests. Figure 14 shows a comparison between simulated beam positions onto the target given a known beam input location and beam positions as measured by the MCP system. The agreement between the two is good but the simulations consistently underestimate the radius of the beam spot's position on the target. Systematic focusing effects in the MCP optics are believed to be responsible for the discrepancy, and because of good agreement between foil tests and modeling results, the Concentrator focusing is believed to be sufficiently well understood that quantification of the mass fractionation of the ions implanted in the target is below the design requirement. One difficulty with the MCP data is that all 3 flat grids must be changed out to install the MCP system necessitating remapping to determine the exact form of each grid each time a change is made.

4.4 Target Implantation

Target implantation, like foil implantation is a check of the fidelity of the full Concentrator system, design, simulation codes, and operation showing for example that grid transparency is as expected. However target implantation also confirms the complete target methodology from target production and handling to the analysis methods to be used for post-flight scientific investigations. Figure 17 shows a target after an implantation has been performed. This target has been archived for future analysis.

5. Components and Component Level Testing

Several specialized components were developed for the Concentrator because of the unusual demands of the instrument's design. Any component not already proven in flight applications had to undergo rigorous testing beyond the standard tests they endured as part of the Concentrator.

5.1 Grids

Extremely strong mesh with the highest possible open area ratio was very important to the overall operation of the Concentrator. Woven mesh was found to be optimal for the Concentrator. This mesh is considerably stronger and more consistent than etched mesh. In order to have sufficient open area, etched mesh must be eroded until it develops weak points in the corners where the etching process invades grain boundaries in the metal. Etched mesh also must be made from a very thin sheet of material so that if the bars of the mesh measure 25µm along the surface they are generally only ~2.5µm normal to the surface. Woven mesh wires are the same thickness in both directions and provide some extra resilience because of the slightly wavy pattern induced by weaving. The mesh in the concentrator is made from 400 series stainless steel wire 25µm in diameter woven on a 20 lines/cm pitch. Pull tests confirmed additional strength from coldworking of the wires when they are drawn and the added ductility of the woven configuration. Immersion of mounted grids and grid samples in liquid N_2 confirmed that there would be no phase change in the material, which might cause dimensional and strength variations when shadowed during spacecraft maneuvers.

5.2 Insulator Coatings

The alumina high voltage standoffs separating the various Concentrator electrode elements are a possible source of field variations. Sunlight striking electro-optical surfaces within the Concentrator will generate photoelectrons, which in some cases will be drawn toward the insulating standoffs because of the orientation of the electric fields around them. Bare alumina has a bulk resistivity $> 10^{16}\ \Omega$, which is sufficiently high that the standoffs may not be able to bleed off the photoelectrons quickly enough to prevent significant charge accumulation and possible voltage breakdown. This effect is generally small and can be studied under normal laboratory testing. However, in the case of insulators with conducting surfaces nearby which will be in full sunlight, raytracing is necessary to determine if photoelectrons deposited on the insulating surfaces result in increased charging and cause unwanted electro-optical effects. This effect cannot be fully tested under laboratory conditions because it requires simultaneous use of a sun source and an ion beam source, which, for high fidelity, requires the use of different test chambers. The maximum electron flux from the solar irradiation of metallic parts onto the insulators can be determined by first calculating the photoelectron production rates for the conducting surfaces and then performing trajectory simulations to determine transport efficiency of the photo electrons to the standoffs. If particle trajectories are disturbed by charging of the standoffs, resistance of the standoffs must be reduced significantly below their bare-alumina values.

Analysis of this effect showed that the only insulators subject to excessive charging are the mirror electrode's edge standoffs which are in the direct path of the photoelectrons ejected from the outer edge of the domed grid and the central standoff between the target and the target sun shade which is struck by ions which miss the target. Approximately 5 nA of photoelectron current must be discharged by the 12 mirror electrode of standoffs, or ~0.5 nA per standoff, which determined that the maximum resistance should be less than 10^{13} Ω per standoff. This is balanced by the need to keep the current drawn from the high-voltage power supply less than the supply limit of 3 μA. This requires that the standoffs have a resistance of at least 10^{10} Ω per standoff. Thus a resistance of about $3x10^{11}$ Ω per standoff between factors of 1/30 and 30 was desired. For the central standoff the resistance required was between 10^{10} and 10^{14} Ω.

The coating chosen for the standoffs was SiC doped with nitrogen. The nitrogen content in the SiC controls the bulk resistivity of the film and the SiC provides a hard, low-oxygen easily-handled surface. The N content is too low to cause concern over possible target contamination from sputtering of this coating. The film is normally deposited by a discharge sputtering method in an argon environment of about 10 mTorr. By adjusting the partial pressure of nitrogen gas in the discharge environment, the nitrogen doping content can be controlled. For the 2.5 μm-thick film used here, the desired nitrogen partial pressure was empirically determined to be 5% in order to achieve the desired resistivity (~10^8 Ω-cm). The coating thickness was determined by the vendor (Technology Assessment and Transfer, Inc.) using profilometry on witness slides. The most critical property of the SiC films is that they do not reduce the resistance between electrodes below the level necessary to operate the high voltage supplies. This was verified during the high voltage functional test of the FM after buildup. The current drawn from the power supplies was monitored to verify that the required level was acceptable. To verify that the standoff resistance is also low enough to bleed off photoelectrons, a representative sample of the coated standoffs was tested to determine the individual resistances of the SiC films. Final resistance of flight standoffs was $5x10^{11}$ Ω for each mirror electrode standoff and $2x10^{13}$ Ω for the target standoff.

To determine if these films had the necessary stability for use in flight, lifetime testing of SiC films on glass slides and on alumina disks were placed in an oven at 80° C while the humidity was held at 100% for a period of 1 month. This simulated conditions prior to launch and is considered a significant over-test of expected environmental conditions. The films were doped with varying percentages of nitrogen partial pressure, ranging from 0 to 40%. Films coated on alumina showed no signs of wear. However to varying degrees, all of the samples on glass slides showed peeling, except for a pure SiC film. Because the films on alumina represent the standoff configuration and the glass slides do not, the failure of the films on glass slides was not considered to be of concern. Two samples of SiC coated on alumina, one at 7% nitrogen partial pressure and the other at 16%, were next exposed to UV radiation from a xenon lamp to simulate solar irradiation. The exposure dosage (intensity x time) was 10 times the UV exposure expected over the mission lifetime. The 7% sample showed no signs of wear, whereas the 16% sample appeared to “fade”, as if the coating had been being ablated. The fading was particularly significant around the edges of the piece. The adherence of the films does not appear to be affected. Both coatings still pass the “tape” test and do not abrade while being rubbed with a latex-gloved finger. The cause of the fading is unknown. The exposure was carried out in air, and more importantly, in a fairly significant ozone environment (the ozone being created by the UV lamp). Thus the fading could either be due to a direct reaction with the UV radiation or a reaction involving the presence of air/ozone. The UV exposure test was considered to be successful for the Concentrator standoffs because the nitrogen partial pressure for coating the flight standoffs was 5%, which is below the 7% partial pressure coating conditions used for the sample that showed no signs of wear. The integrity of the coatings is expected to increase at lower nitrogen pressures as their composition becomes more like pure SiC. Thus, flight standoff coatings have wear properties that are as good as or better than the 7% sample. Neither the mirror standoffs nor the central target support standoff are directly illuminated in normal Concentrator operation. Finally, the tested exposure was a factor of 10 in excess of the expected dose, and in the unlikely event that some ablation occurs, it should be very much less than that in our testing. Figure 18 shows the coated mirror electrode standoffs.

6. Operation

The Concentrator voltages are adjusted in real time onboard to react automatically to changes in the solar wind. However, Concentrator voltages should not be changed too rapidly and consequently have limited deltas on existing potentials. Defining $\Delta V_? = (V_?)_n - (V_?)_{n-1}$ where $(V_?)_n$ is the desired new voltage and $(V_?)_{n-1}$ is the readback voltage of the present CEB setting then $|\Delta V_?| \leq 500$ V. If the desired change is more than 500 V, the CEB will catch up after 2 or more cycles of 5-30 (nominally 30) seconds. The acceleration voltage will remain at –6.5 kV during normal operation. The mirror and hydrogen-rejection grid voltages are set based on the peak in the proton energy distribution, Ep. Ep is a running average of the last three consecutive measurements of Ep defined as

$$Ep = (Ep_n+Ep_{n-1}+Ep_{n-2})/3$$

to help smooth out any noise from individual measurements. The mirror voltage is

$$V_M = Ep*4.32$$

as described in the Overview section. The hydrogen rejection-grid is set at

$$V_H = Ep* R$$

where R is given in Table IV. The operational settings of the concentrator are archived along with the solar wind moments from the monitors, so that the concentrator target samples will be understandable in the context of the solar wind conditions experienced during the mission.

7. Summary

The extremely demanding scientific and operational requirements placed on the Concentrator have all been met. Table II gives a complete list of performance requirements for the flight Concentrator. Many types of testing and characterization were used to verify that all of these criteria have been met. In order of the listing in Table II here are the results of these tests and the expected performance of the Concentrator.

1. The concentration factor varies for the type of solar wind encountered and reaches a maximum of 22.8 for low-speed solar wind. The worst case is 16.8 for high speed solar wind which occurs ~1% of the time. The concentration factor is calculated as follows:

Geometric Factor = $(\text{Aperture Radius})^2 / (\text{Target Radius})^2 = (20\text{ cm})^2/(3.1\text{ cm})^2 = 41.6$

Grid Transmission = $(\text{Grid Open Area Ratio})^{(\text{Number of grids traversed})} = (0.9044)^5 = 0.605$

Fraction Hitting Target = 0.669 to 0.907 from simulations

Concentration Factor = Geometric Factor * Grid Transmission * Fraction Hitting Target = 16.8 to 22.8

The fraction of ions hitting the target will be determined by SIMION for the solar wind conditions encountered. Thus the expected integrated concentration factor is over 20 but will depend on the exact solar wind conditions encountered.

2. Sufficient target area is needed to allow several analyses of the target material and archival of ≥50% for future analysis. This required a target area of $\geq 15\text{ cm}^2$. The measured target active area in the Concentrator is 25.9cm^2. While this is relatively large, the concentration of ions in the target decreases as a function of radius so that the most desirable portions of the target will be the inner $\sim 15\text{cm}^2$. Figure 6 shows the target assembly including the alternating wedges of SiC and diamond. These different materials have different background contamination levels of the elements and isotopes of interest and the separate analyses and background levels should allow for more verifiable results.
3. The Concentrator must focus ions with widely varying charge state and velocity distributions into its target without introducing unknown variations and, thus, analysis errors, in the implanted $^{17}\text{O}/^{16}\text{O}$ ratio different from that in the solar wind by greater than 0.1%. Implantation variations can be calculated with SIMION before flight to this level and will be checked after flight with Ne^+ implantation levels. Details of the simulations used to verify this level of operation are given in Wiens et al. 2002.
4. The Concentrator target temperature must not exceed 250°C to avoid damage to the target material and release of the implanted species. The calculated worst-case temperature is 230°C.
5. To further avoid damage to the target from hydrogen buildup, 90% of Solar wind proton fluence must be prevented from reaching the target. Figure 4 shows that with the planned operational methodology the current design rejects ~93%.
6. Concentrator cleaning, coating, handling, and final cleaning methods have been verified to have a surface contamination by C, N, O below 10^{15} atoms/cm^2 under ultra high vacuum ($<10^{-8}$torr) conditions at 200ºC. The level of contamination was continually monitored in all operations before flight by the use of witness plates. In addition, the Concentrator underwent a final cleaning and gold coating after all

> testing was complete and just before flight to eliminate any possibility of contamination during handling. Both of these operations had been previously analyzed and found to meet the contamination design specification. Once in flight, contaminates do not implant and the outer layer of the targets will be removed before analysis of the implanted solar wind is performed.

The FM Concentrator in its final configuration for flight is shown in Figure 19. We look forward to the return of the Concentrator and its targets. Upon retrieval the Concentrator will be returned to Los Alamos National Laboratory for analysis of its operation with the mapping facility, the targets will be removed under ultra-clean conditions, and then the Concentrator will be tested in the ion beam facility. If the midair capture of the sample-return canister fails we expect that there will be some damage to the Concentrator that may make mapping and operation in the ion beam impossible but we expect to retrieve the target pieces intact.

8. Concentrator Design Parameters

Overall diameter	46 cm
Overall height, excluding CEBs	21 cm
Working aperture	40 cm
Target diameter	06.2 cm
Focal length, mirror electrode	21.7 cm
Focal length, domed grid frame	14.0 cm
Mirror grid stand-off from electrode	≥2.5 cm
H-grid to ground grid stand-off	0.6 cm
Acceleration grid to H-grid stand-off	1.8 cm
Domed Grid to Acceleration Grid at Center	14.35 cm
Domed Grid to Target at Center	13.85 cm

Electrode microstep height	100 microns

Concentrator mass, excluding CEBs	6.0 kg
HVPS mass, (CEBs, each of two)	1.4 kg

Maximum allowable target temperature	250°C
CEB operating thermal range	-10/+77°C
CEB survival thermal range	-15/+77°C

Ground Grid Aperture	41.6 cm
Domed Grid Aperture	40.0 cm
Mirror Electrode Diameter	41.9 cm
Angle of electrode at edge, relative to normal	25.8 °

Offset angle relative to canister	0°

Acceleration potential	-6.5 kV
H grid potential range	0.1 to 3.5 kV
Mirror Electrode potential range	2.0 to 10.0 kV
Nominal H grid potential	~1.3*Ep
Nominal mirror potential	4.32*Ep
H grid steps	0.855 V linear
Mirror electrode steps	2.44 V linear

Desired solar wind velocity range	300-800 km/s
Desired solar wind energy range	0.47-3.34 keV/amu
Desired solar wind m/q range	2.0-3.6

Mirror penetration for (hypothetical) ions normally incident at center (% of distance from grid to electrode)

m/q = 2.0 ($^{16}O^{+8}$):	83.8%
m/q = 3.6 ($^{18}O^{+5}$):	95.0%

References

Bochsler, P., and Geiss, J.: 1989, ‘Composition of the solar wind’, in *Solar System Plasma Physics, Geophysical Monograph 54* eds. J. H. Waite, Jr., J. L. Burch, and R. L., Moore, 133-141.

Clayton, R.N.: 1993, ‘Oxygen isotopes in meteorites’, *Ann Rev. Earth Planet Sci*. 21, 115-149.

Collier, M.R., Hamilton, D.C., Gloeckler, G., Ho, G., Bochsler, P., Bodmer, R., and Sheldon, R.: 1998, ‘Oxygen 16 to oxygen 18 abundance ratio in the solar wind observed by WIND/MASS’, *J. Geophys. Res.* 103, 7.

Barraclough, B. L., Dors, E. E., Abeyta, R. A., Alexander, J. F., Ameduri, F. P., Baldonado, J. R., Bame S. J., Casey P. J., Dirks, G., Everett D. T., Gosling, J. T., Grace, K. M., Guerrero, D. R., Kolar, J. D., Kroesche, J., Lockhart, W., McComas, D. J., Mietz, D. E., Roese, J., Sanders, J., Steinberg, J. T., Tokar, R. L., Urdiales, C., and Wiens, R. C.: 2002, ‘The Plasma Ion and Electron Instruments for the Genesis Mission’, *Spa. Sci. Rev.*, this volume.

Bochsler, P.: 2000, ‘Abundances and Charge States of Particles in the Solar Wind’, *Reviews of Geophysics* 38, no. 2, 247-266.

Bodmer, R. and Boschler, P.:2000, ‘Influence of Coulomb collisions on isotopic and elemental fractionation in the solar wind acceleration process’, *J. Geophys. Res.* 105, no. A1, 47-60.

Bühler, F., Eberhardt, P., Geiss, J., Miester, J., and Signer, P.: 1969, ‘Apollo 11 Solar Wind Composition Experiment: First Results’, *Science* 166, no. 3912, 1502-1503,

Bühler, F., Geiss, J., Miester, J., Eberhardt, P., Huneke, J.C. and Signer, P.: 1966, ‘Trapping of the Solar Wind in Solids’, *Earth and Planetary Science Letters* 1, 249-255.

Burnett, D. S., Barraclough, B. L., Bennett, R., Neugebauer, M., Oldham, L. P., Sasaki, C. N., Sevilla, D., Smith, N., Stansbery, E., Sweetnam, D., and Wiens, R. C.: 2002, ‘The Genesis Discovery Mission: Return of solar matter to Earth’, *Spa. Sci. Rev.,* submitted for this issue.

Geiss, J., Eberhardt, P., Signer, P., Bühler, R., and Meister, J.: 1969, ‘The Solar Wind Composition Experiment’, Section 8 of *Apollo 11 Preliminary Science Report*, NASA SP-214, 183-186.

Geiss, J., Eberhardt, P., Bühler, R., Meister, J., and Signer, P.: 1970, ‘Apollo 11 and 12 Solar Wind Composition Experiments: Fluxes of He and Ne Isotopes, *J. Geophys. Res.* 75, no. 31, 5972-5979.

Geiss, J., Bühler, R., Cerutti, H., Eberhardt, P., and Filleux, Ch.: 1972, 'Solar Wind Composition Experiment', Section 14 of *Apollo 14 Preliminary Science Report*, NASA SP-315, 14-1 – 14-10.

Harris, M.J., Lambert, D.L., and Goldman, A.: 1987, 'Carbon and oxygen isotope ratios in the solar photosphere', *Mon. Not. R. Astr. Soc*. 224, 237.

Jurewicz, A. J. G., Burnett, D. S., Wiens, R. C., Friedmann, T. A., Hays, C. C., Hohlfelder, R. J., Nishiizumi, K., Stone, J. A., Woolum, D. S., Becker, R., Butterworth, A. L., Campbell, A. J., Ebihara, M., Franchi, I. A., Heber, V., Hohenberg, C. M., Humayun, M., McKeegan, K. D., McNamara, K., Meshik, A., Pepin, R. O., Schlutter, D., and Wieler, R.: 2002, 'Overview of the Genesis solar-wind collector materials', *Spa. Sci. Rev.*, this volume.

Kallenbach, R., Geiss, .J., Ipavich, FM., Gloeckler, G., Bochsler, P., Gliem, F., Hefti, S., Hilchenbach, M., and Hovestadt, D.: 1998, 'Isotopic composition of solar wind nitrogen: First in situ determination with the CELIAS/MTOF spectrometer on board SOHO', *Astrophysical Journal* 507, no. 2, pt. 2, L185-L188.

Kallenbach, R., Ipavich, FM, Bochsler, P., Hefti, S., Hovestadt, D., Grunwaldt, H., Hilchenbach, M., Axford, WI., Balsiger, H., and Burgi, A.: 1997, 'Isotopic composition of solar wind neon measured by CELIAS/MTOF on board SOHO', *Journal of Geophysical Research-Space Physics* 102, no. A12, 26895-26904.

McComas, D.J., et al.: 1998,'Solar Wind Concentrator', *Measurement Techniques for Space Plasmas,* R.F. Pfaff, J.E. Borovsky, D.T. Young, AGU Monograph 102, 195-200.

Neugebauer, M., Steinberg J.T., Tokar R.L., Barraclough B.L., Dors E.E., Wiens R.C., Gingerich D.E., Luckey D., and Whiteaker D.B.: 2002, 'Genesis on-board determination of the solar wind flow regime', *Spa. Sci. Rev.*, this volume.

Pepin, RO:1991, 'On The Origin And Early Evolution Of Terrestrial Planet Atmospheres And Meteoritic Volatiles', *Icarus* 92, no. 1, 2-79.

Signer, P., Eberhardt, P., and Geiss, J.: 1965, 'Possible Determination of the Solar Wind Composition', *J. Geophys. Res* 70, no. 9, 2243-2244.

Wiens, R.C., Huss, G.R., and Burnett, D.S.: 1999, 'The solar oxygen-isotopic composition: Predictions and implications for solar nebula processes', *Met. Planet. Sci.* 34, 99.

Wiens, R.C., Neugebauer, M., Reisenfeld, D.B., Moses, R.W., Jr., and Nordholt, J.E., Burnett, D.S.: 2002, 'Genesis Solar Wind Concentrator: Computer simulations of performance under solar wind conditions', *Spa. Sci. Rev.*, this volume.

Wimmer-Schweingruber, R.F., Bochsler, P., and Gloeckler G.: 2001, 'The isotopic composition of oxygen in the fast solar wind: ACE/SWIMS', *Geophys. Res. Lett.* 28, no.14, 2763-2766.

Acknowledgements

The authors would like to acknowledge NASA contract number W-19,272 for supporting this work. The design, development, and construction of the Concentrator would not have been possible without the help of many individuals. The authors would like to thank the following outstanding individuals: Diane Albert, Frank Ameduri, Matt Anderson, Richard Bramlett, Randy Edwards, Brian Henneke, James Lake, and Stacy Rupiper of Los Alamos National Laboratory; Dennis Guerrero, Irene Arevalos, Greg Dirks, Jeff Roese, Toby Stecklein, Jack Taguiam, Syrrel Rogillio, and James Sanders of the Southwest Research Institute; Chet Sasaki, Virgil Mireles and Don Sevilla of the Jet Propulsion Laboratory; Lada Adamac of Caltech; Allen Dorn of Screen Technology Group; Jerry Spieckerman of Marketech, Inc.; Steve Good of Reynolds Industries, Inc.; Kenneth Bedard formerly of Precimeter, Inc.; and David King and Joseph Maciejewsky of Technology Assessment and Transfer, Inc., Wear Sciences Division.

Tables:

Element	**Solar wind abundance, atomic fraction**	**Expected concentration given 20x concentration factor**
N	8x10^{-5}	4x10^{18}/cc
O	5x10^{-4}	3x10^{19}/cc
F	~20ppb	1x10^{15}/cc
Ne	9x10^{-5}	4x10^{18}/cc

Table I. Target implantation levels expected in the Concentrator. Concentrations refer to average over outer 100 nm for a 26 month exposure. Abundance fractions from Bochsler and Geiss (1989)

Performance parameter	**Value Required**	**Value Achieved**	**Comments**
Average Concentration Factor for N and O	≥20	22.8	Low speed solar wind
		20.9	Weighted average over all expected solar wind speeds
Target Area	≥15 cm^2	25.9cm^2	
Errors in ^{17}O/^{16}O	0.1%	0.085%	Calculated with SIMION before flight to this level Checked after flight with Ne$^+$ implantation levels
Target Temperature	≤250°C.	230ºC	Worst case calculated temperature; EM STV test target frame = 144 deg C
Ion Acceleration Before Impacting Target	>5 Kv	10kV possible see text	Operation at 6.5 kV
Solar Wind Proton Fluence Prevented From Reaching Target	≥90%	≥93%	Averaged over all thermal Mach numbers
Surface Contamination by C, N, O	<10^{15} atoms/cm^2 under ultra high vacuum (<10^{-8}torr) conditions at 200ºC		Concentrator gold coating approved. Grids not coated calculations show minimal implantation resulting Inflight contaminates do not implant

Table II. Concentrator performance requirements.

Isotope	**Charge-state**	**m/q**
H	1	1.0
^{4}He	2	2.0
^{16}O	8	2.0
^{18}O	8	2.25
^{18}O	5	3.60
^{22}Ne	8	2.75
^{56}Fe	9	6.22

Table III. Some isotopes, charge-states, and m/q ratios found in the solar wind.

H rejection voltage $V_H = Ep^* R$

$M^2 = mv^2 / 2kT$

Ep is the peak in the proton energy distribution averaged over the last three consecutive measurement cycles.

M	**R**
> 11	1.3
11>M>9	1.2
9 ≥M≥ 8	1.1
8 >M >6	1.0
≥6	0

Table IV. The voltage setting on the hydrogen-rejection grid will be determined from the peak of the proton energy distribution and the thermal Mach number determined from the solar wind data provided by the Genesis Ion Monitor (Barraclough et al.,2002).

Component	**JPL EM Test**
	°C
Target Shade	93
Target Frame	144
Mirror	132
Accel. Can	105
Accel Frame, in	122
Accel Frame, out	105

Table V. Temperatures measured at different parts of the Concentrator during solar thermal vacuum testing.

Electro-optic component	Typical operating voltage	Maximum CEB voltage	EM Test voltage
Hydrogen-Rejection grid	1.0kV (variable, 2.5 minute timescales)	3.5kV	4.55kV
Acceleration Can	-6.5kV (fixed in flight)	-10kV	-13kV
Mirror Electrode	4kV (variable, 2.5 minute timescales)	10kV	13kV

Table VI. Concentrator voltages.

	Portion of Target	Measured Fraction	SIMION
He*	Inner 1 cm	0.64	0.63
	Middle 1 cm	0.31	0.30
	Outer 1 cm	0.06	0.07
Ne*	Inner 1 cm	0.99	1.00
	Middle 1 cm	0.00	0.00
	Outer 1 cm	0.01	0.00

Table VII. Comparison of Implanted Ions with SIMION Simulations

*Test conducted with EM. He and Ne were implanted with 140 mm straight line scans. For He the scan was perpendicular to and bisecting a radial arc at R = 121 mm. For Ne the scan was nearly radial, near a support rib, from R = 50 to 190 mm. All scans used normally incident 9 kV beams with mirror and acceleration voltages at +/-10 kV, respectively. All noble gas measurements were corrected for backscattering losses.

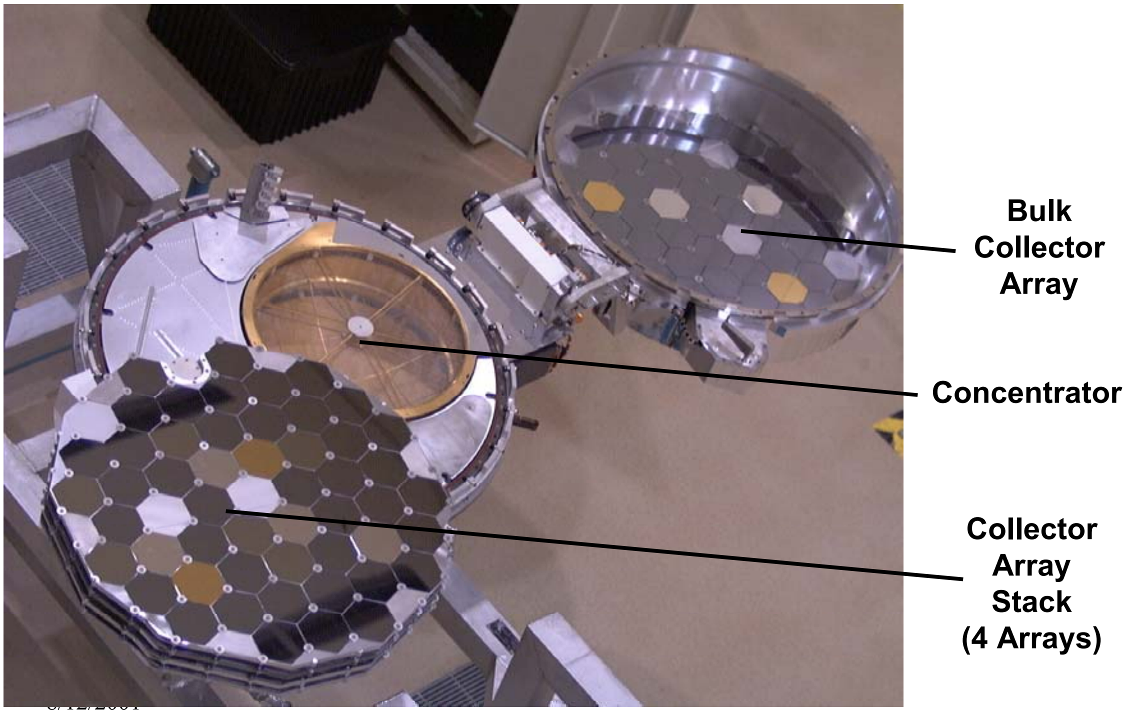

Figure 1. The Concentrator in its flight configuration is visible inside the science canister. During the spacecraft's journey to and return from the L1 point and during the re-entry into Earth's atmosphere the collector arrays are stowed over the Concentrator and the lid containing the bulk collector array is closed forming an airtight seal to protect the exposed samples from contamination.

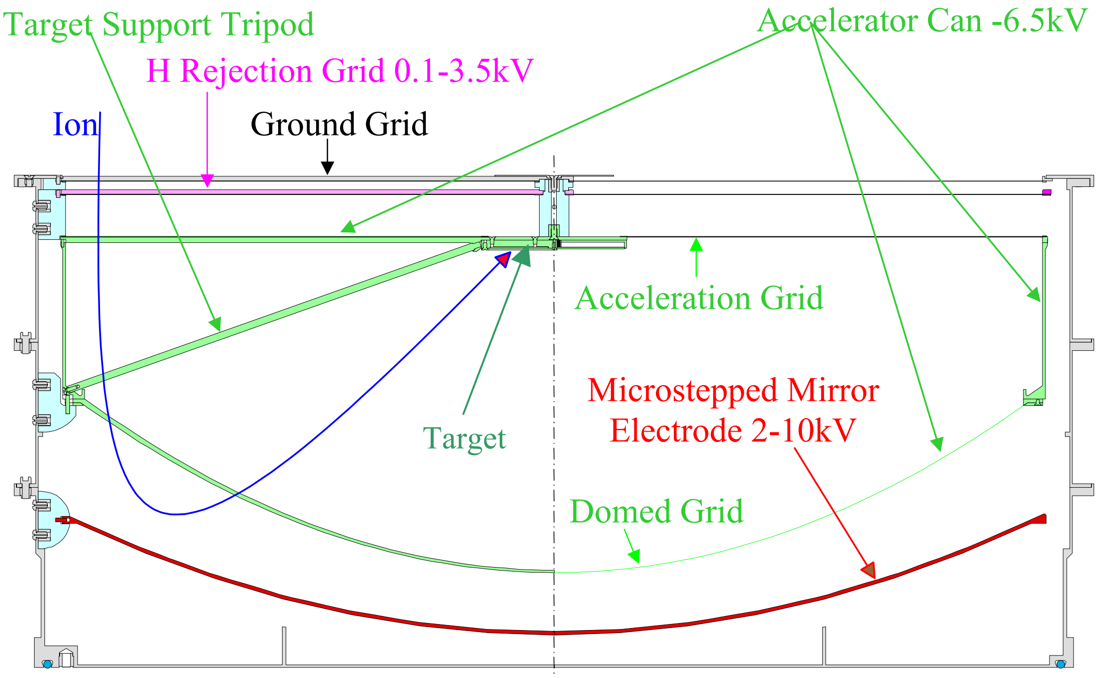

Figure 2. Cross-section of the Concentrator showing the major elements of its design. Electro-optic elements that share voltage levels are color coded to indicate which parts are electrically connected. The left-hand side shows a cross-section through the grid supports and insulators, while the right-hand side shows the cross section between insulators and grid support ribs.

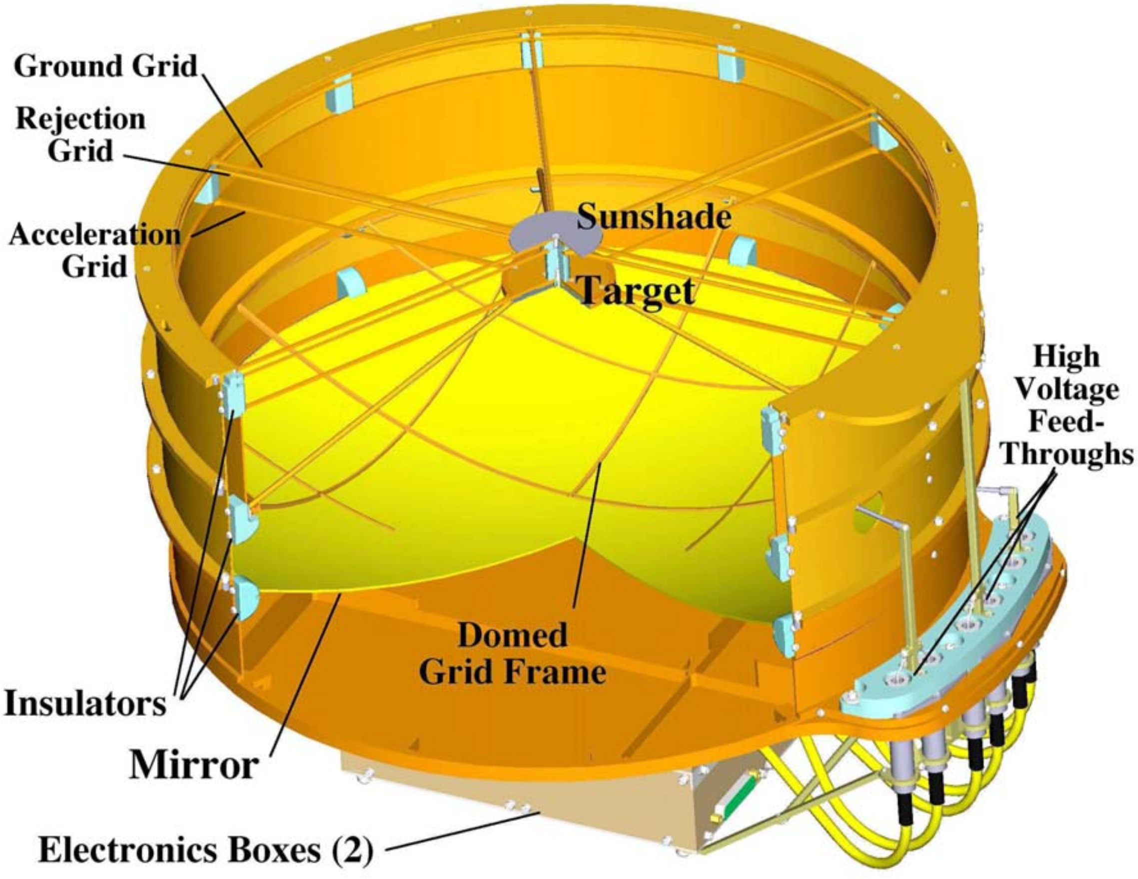

Figure 3. Three dimensional cut-away view of the Concentrator showing its major mechanical and electro-optical components (for clarity only the grid supports and not the grids themselves are shown). The Concentrator electronics boxes and the cabling leading from them to the hermetically sealed high-voltage feed-throughs and the high voltage input section where voltage is distributed to the Concentrator's electro-optical elements are clearly visible. The high voltage input section is shown without its cover which is attached to the outer skin of the Concentrator for flight.

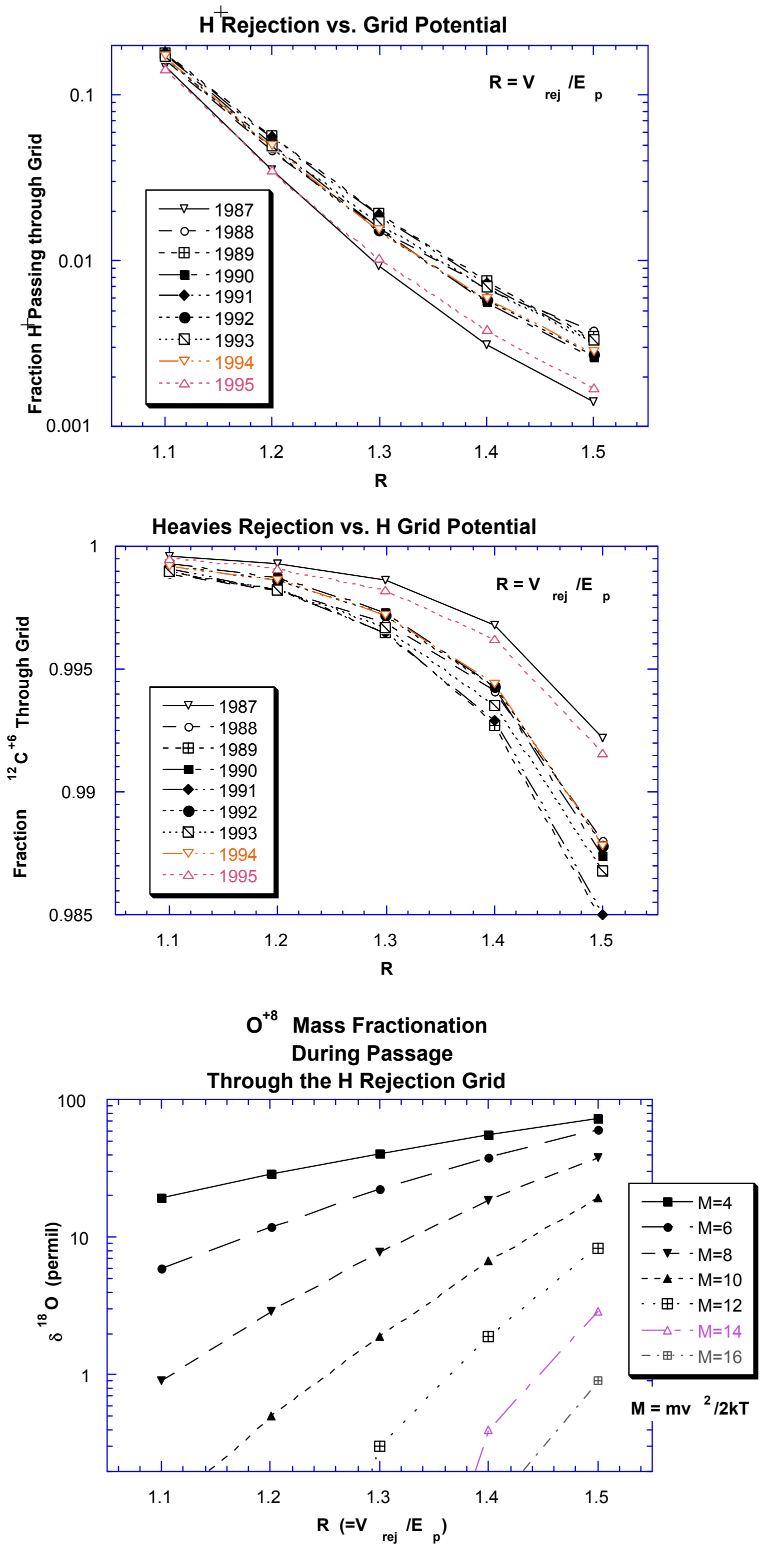

Figure 4. The upper panel shows the fraction of H^+ rejected by the hydrogen-rejection grid for a given ratio, R. The middle panel shows the expected loss of $^{12}C^{+6}$ ions vs. R. With an m/q of 2.0 amu/charge, $^{12}C^{+6}$ is indicative of the worst-case losses induced by the hydrogen-rejection grid. C itself cannot be measured in the Concentrator targets which all have C as a component. The lower panel shows the mass fractionation of O introduced by the hydrogen-rejection grid as a function of ratio and thermal Mach number. These panels give the calculated effects of the hydrogen-rejection grid for average solar wind conditions for the years 1987-1995.

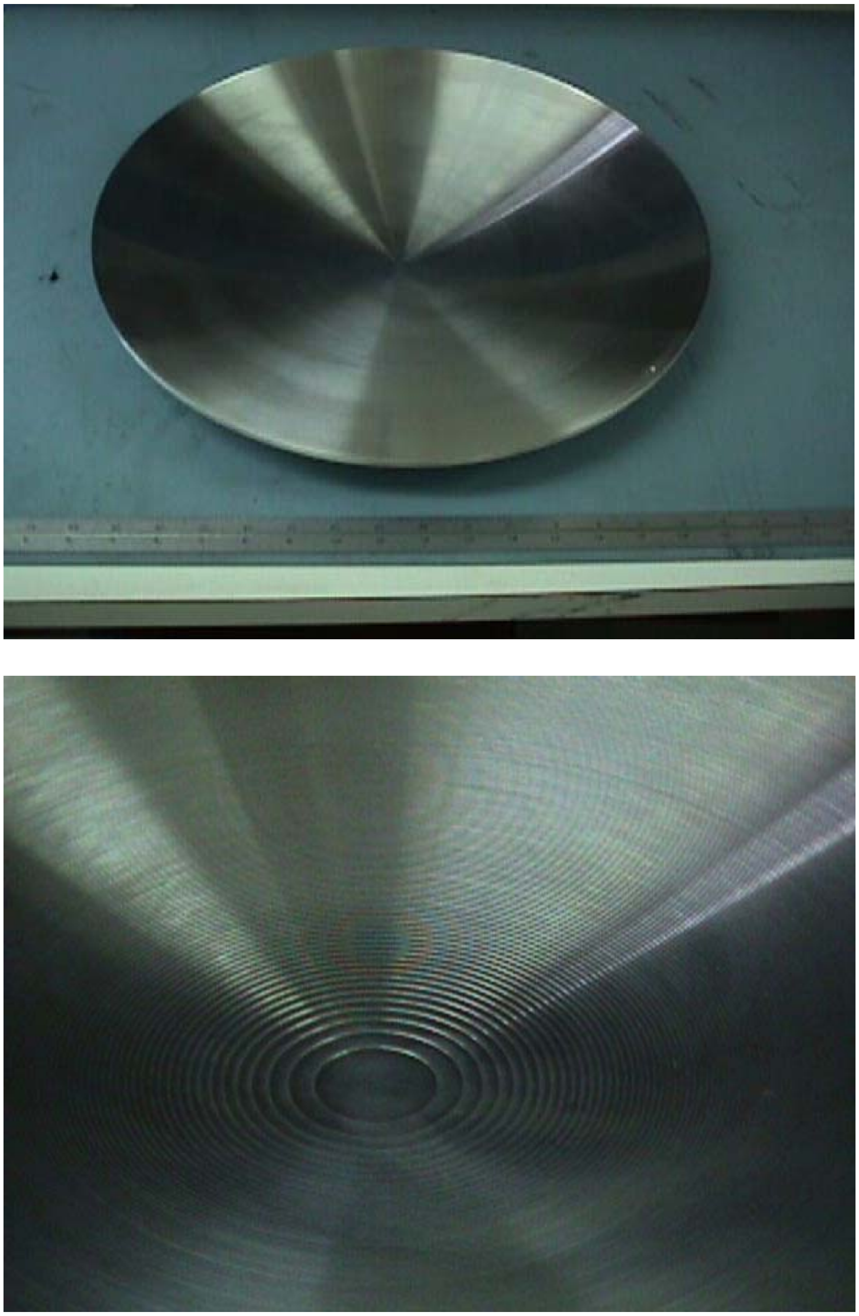

Figure 5. The Concentrator's mirror electrode which can be operated at up to +10kV to produce, in conjunction with the domed mirror grid, a reflecting field which focuses ions onto the Concentrator target. The bottom panel shows an enlarged view of the mirror's center where the microstepping, which prevents this electrode from focusing light onto the target, can be seen most easily.

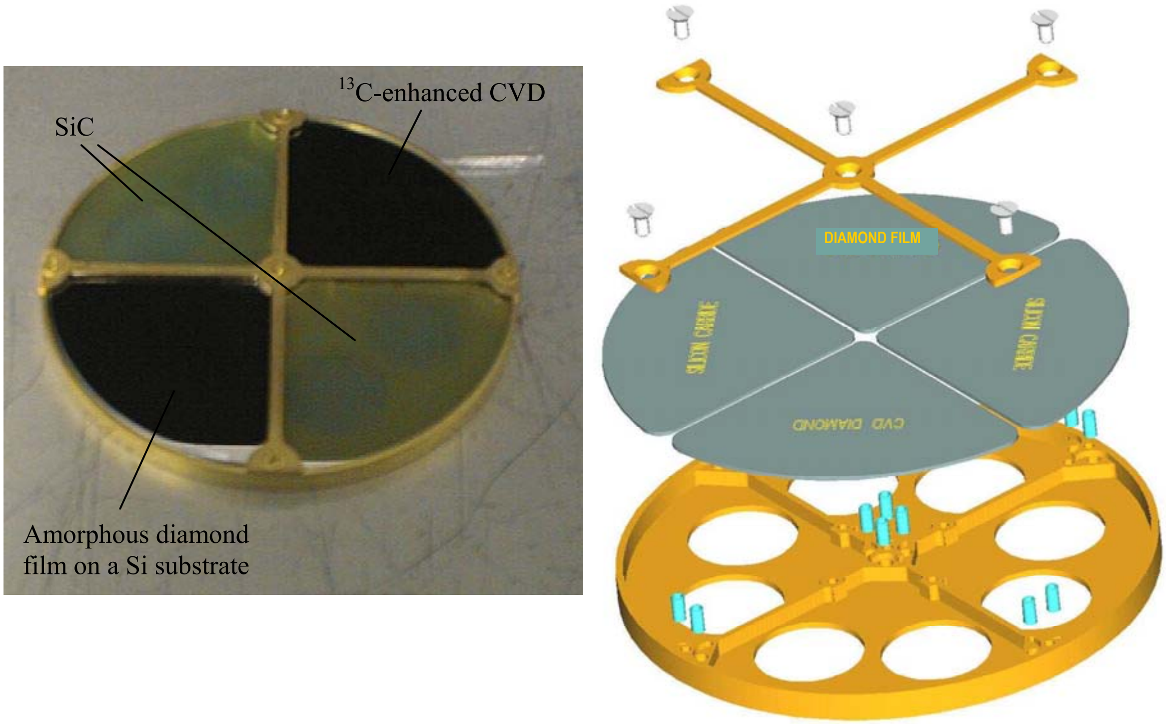

Figure 6. The Concentrator target is shown fully assembled at left and in an exploded engineering drawing at right. The SiC, CVD diamond, and amorphous diamond film on Si sections are clearly visible. The drawing on the right labels the sectors as they are arranged in the flight configuration. Also visible in blue in the drawing at right are the springs which apply force to the corners of the target sectors holding them firmly during vibration.

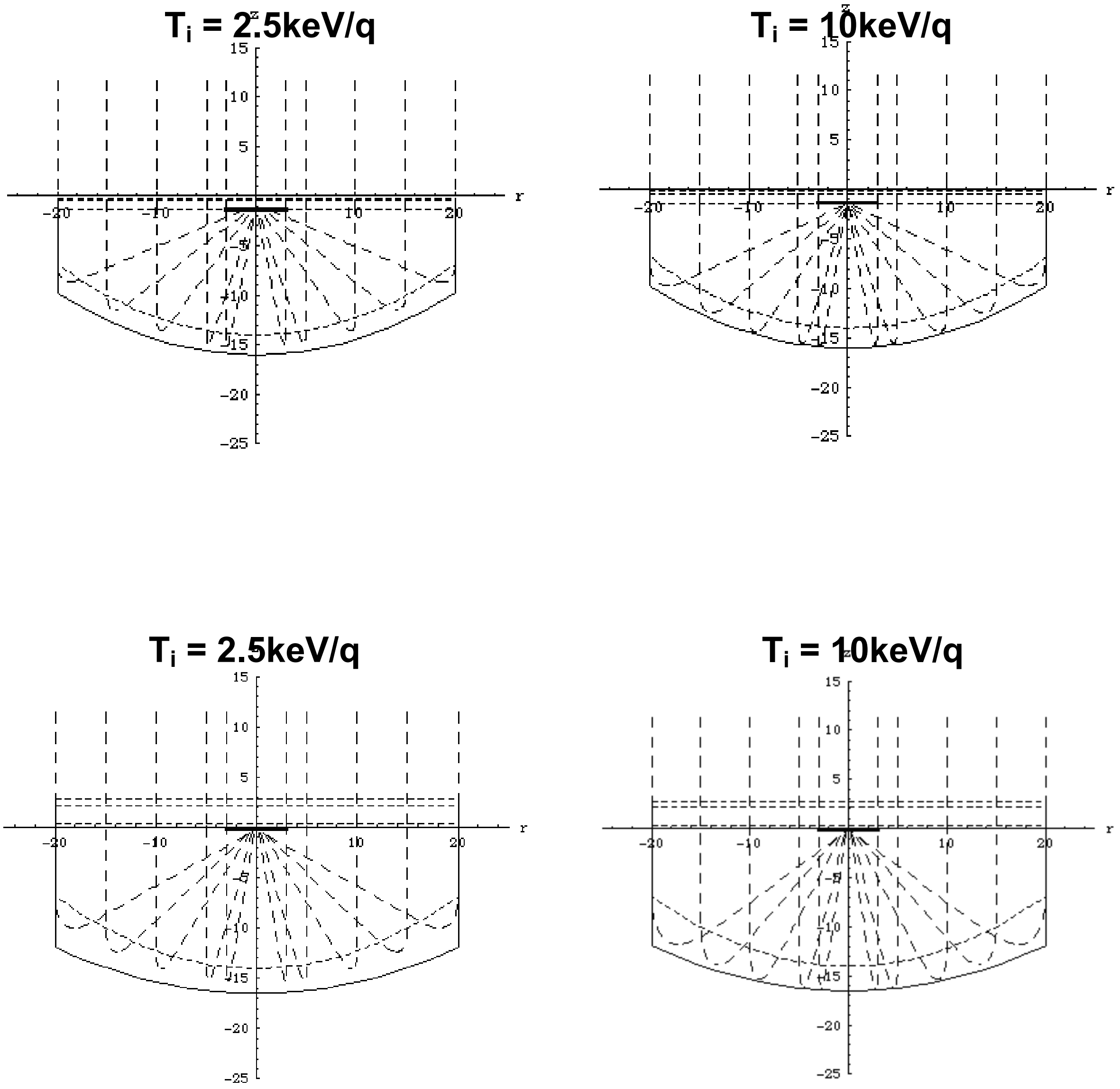

Figure 7. Comparison of Concentrator electro-optical designs for ions of different energies. The design in the upper two panels uses confocal parabolas for the domed grid and mirror electrode, but it is energy-dependent. Although it focuses ions with incident energy of T_i = 10keV/q it focuses poorly at 2.5keV/q. The Concentrator's optimized design which maintains its focus over all input energies is shown in the lower two panels. This design drastically reduces the expected isotopic fractionation.

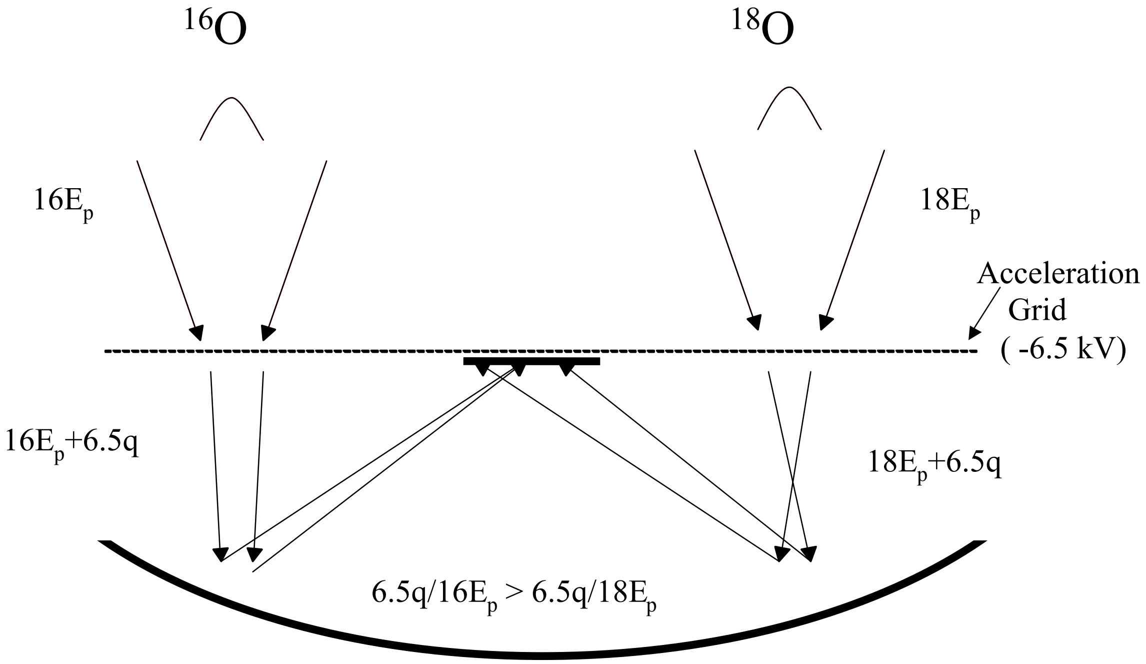

Figure 8. An exaggerated drawing illustrating the different effects of the acceleration grid on ^{16}O than ^{18}O. External to the Concentrator the isotopes have the same angular distribution, but the acceleration grid is more effective at straightening the distribution of ^{16}O. ^{16}O is then more tightly focused than ^{18}O, leading to a fractionation gradient on the target, with more ^{16}O concentrated at the center.

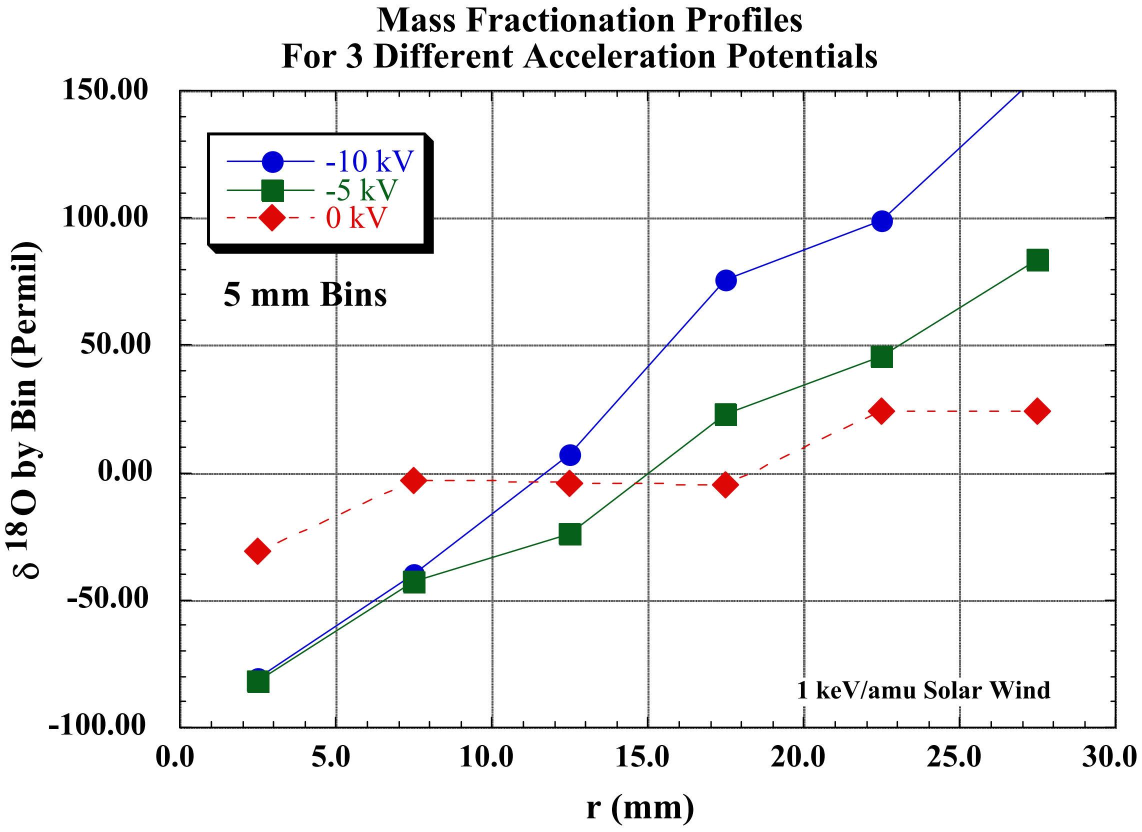

Figure 9. The permil mass fractionation of ^{18}O at a given radius across the target as produced by different operating voltages on the acceleration grid. The simulation used a perfect parabola rather than the actual mirror grid shape, and as such it is a worst case illustration of the effect of the accleration grid (cf. Wiens et al., 2002).

\

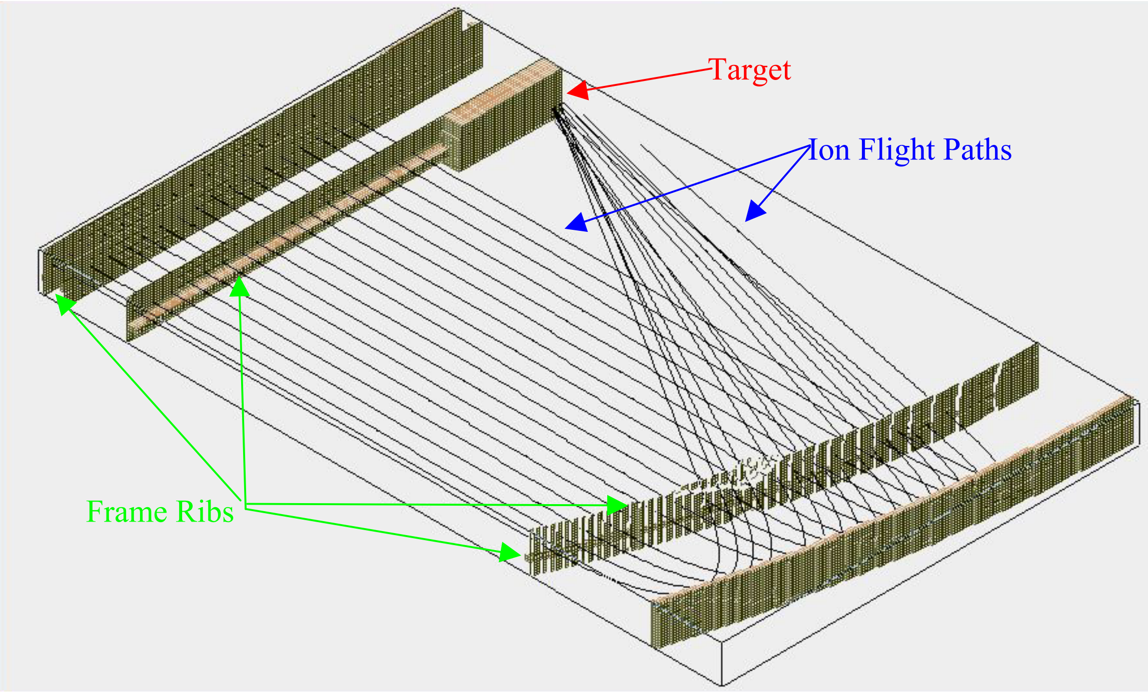

Figure 10. A cross sectional view of the Concentrator as it is modeled in SIMION. Ribs supporting each of the four grids can be seen along with the paths of several ions showing their reflection in the mirror region and implantation into the target.

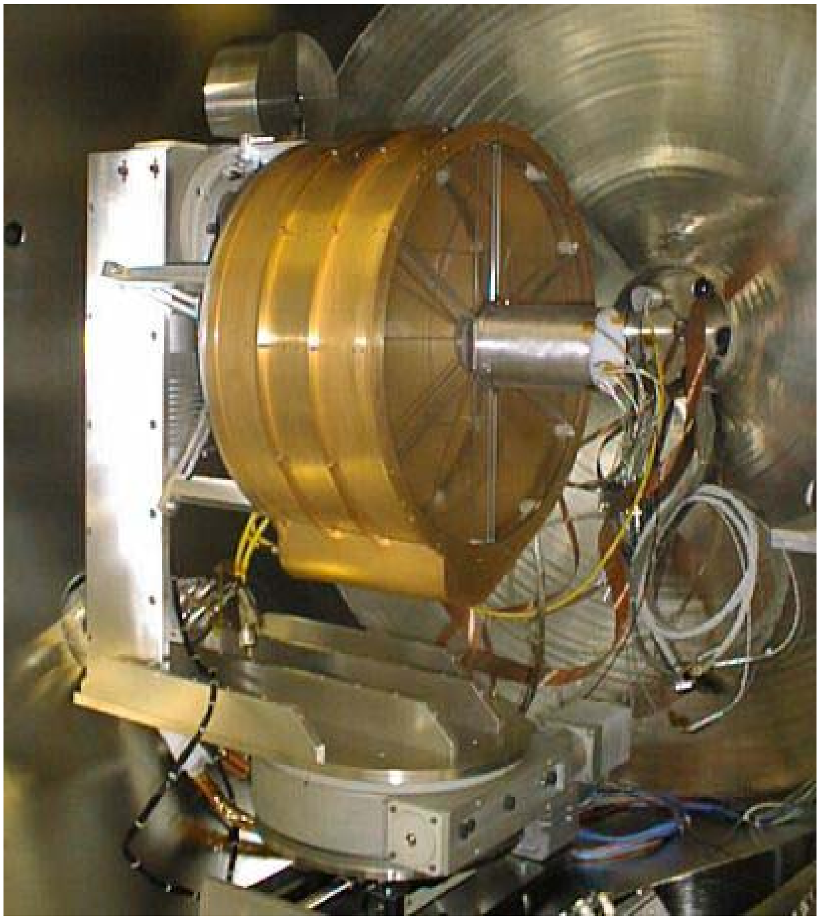

Figure 11. The EM Concentrator is installed in the ion beam test chamber. The central MCP assembly and cable harness can be seen inside a metal cover used to prevent stray fields from this assembly from causing deviations to incoming ion trajectories.

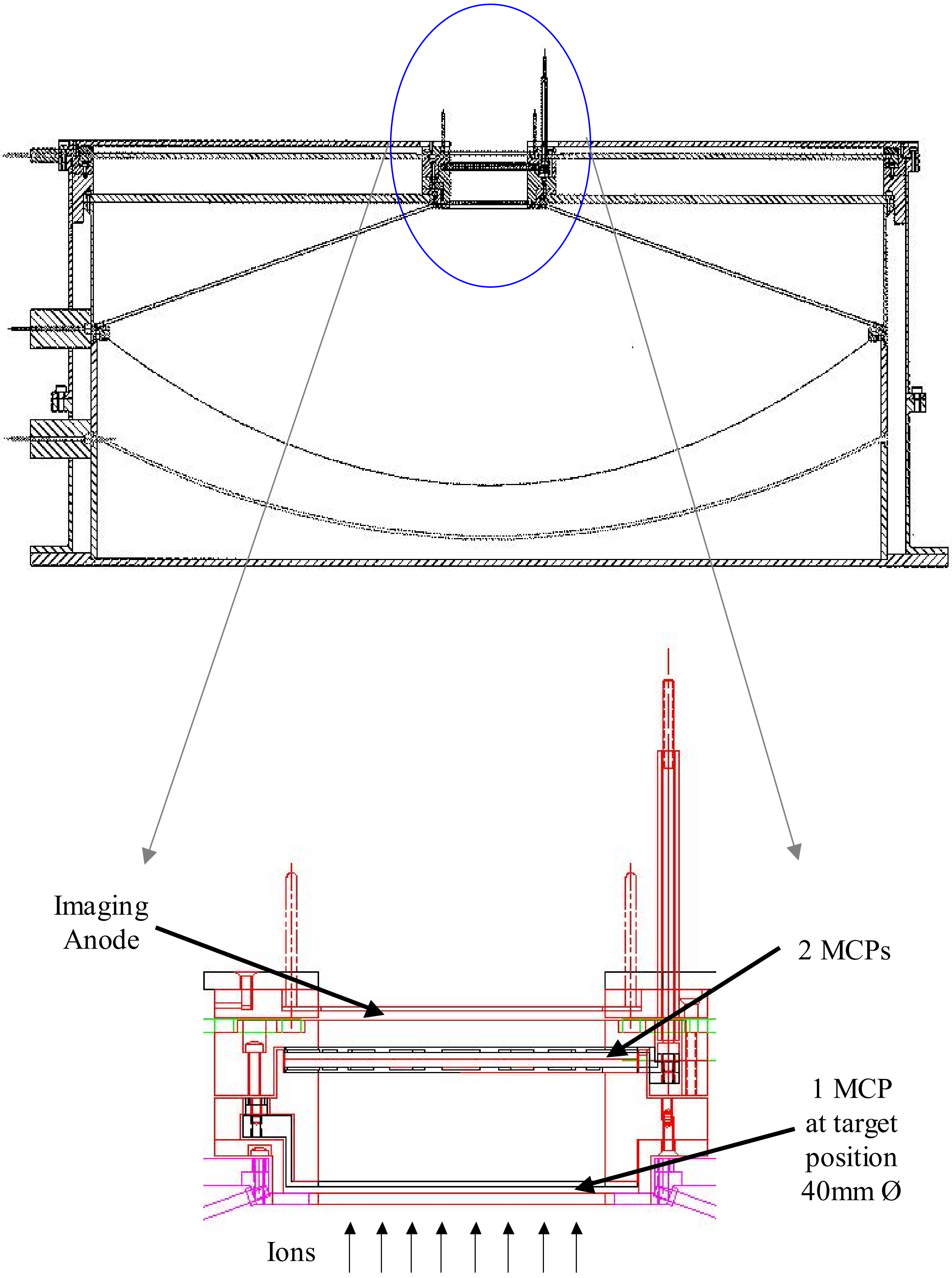

Figure 12. The upper panel shows a cross section of the Concentrator with the MCP imaging assembly installed. The bottom panel shows an enlarged view of the MCP assembly itself. The large vertical structures at the sides of the bottom illustration are the high voltage input pins needed to power the MCP stack.

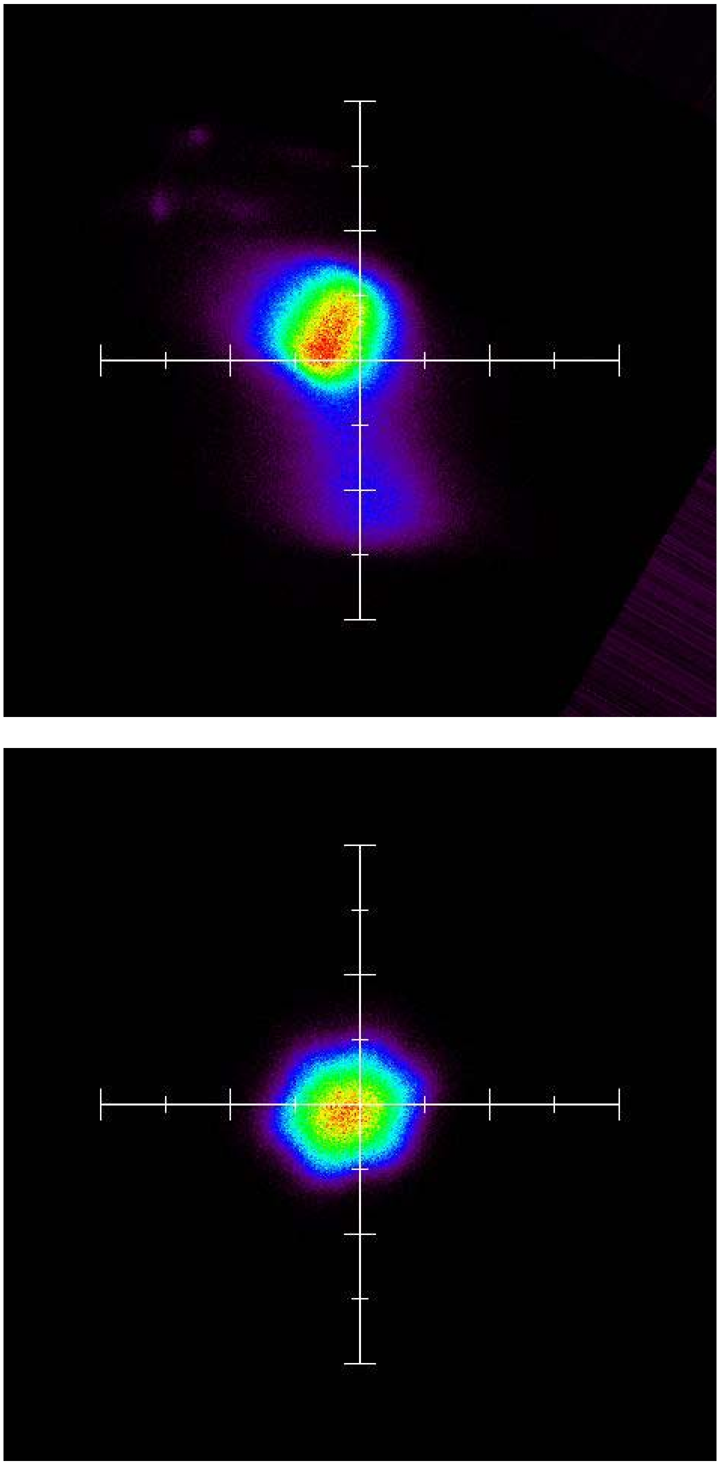

Figure 13. Two ion beam images produced with MCP assemblies. The upper panel shows an image of the beam before entering the Concentrator. The lower panel shows the same beam as it impinges on the MCPs at the target location. The hexagonal shape is due to refraction off the hexagonal etched grid used in the prototype and is only observed when the voltage on the rejection grid is nearly equal to the incident ion energy.

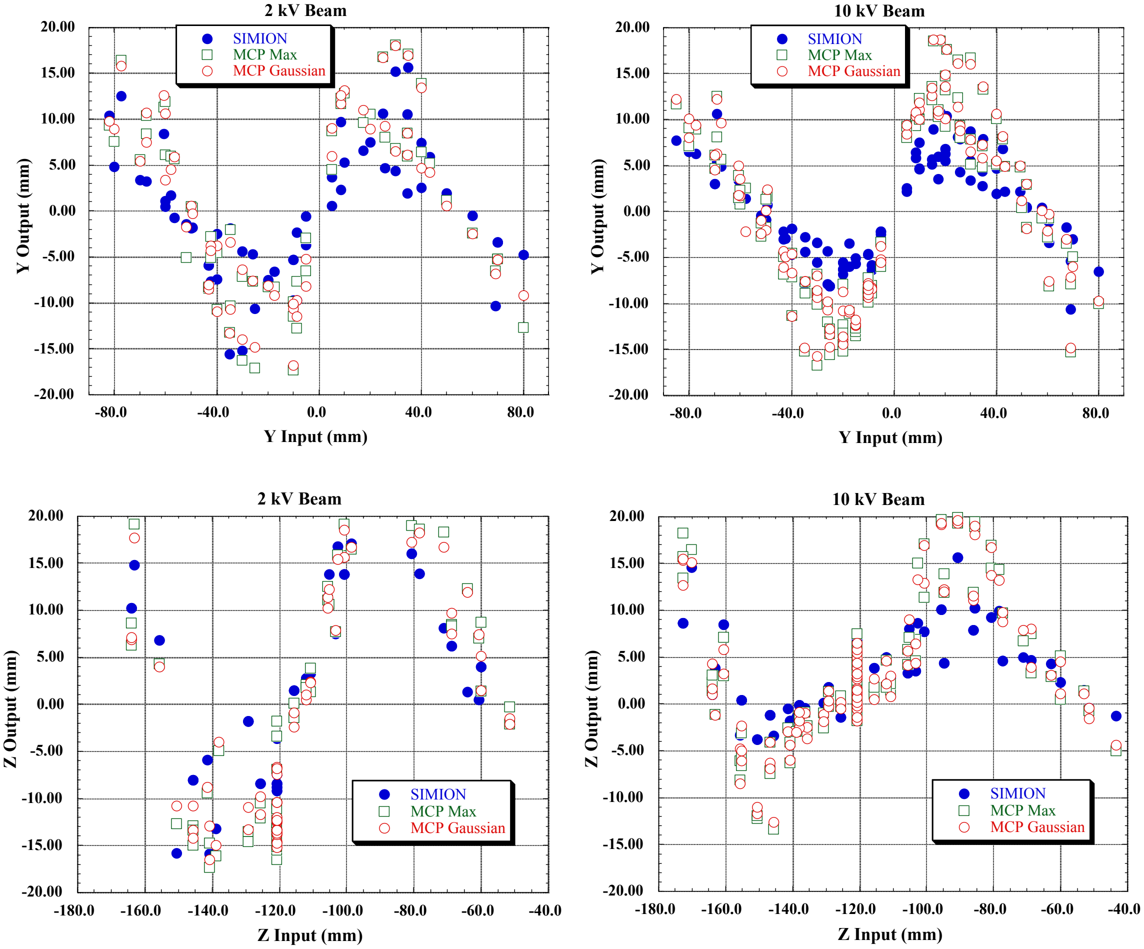

Figure 14. Comparison of the SIMION-predicted location of ion beams on the target and the location determined from the MCP imaging system data vs. the input beam position. The Y and Z-axes are orthogonal directions parallel to the surface of the target. Despite the use of mapping data in the SIMION calculations, there is a systematic under-prediction of the radial spot location.

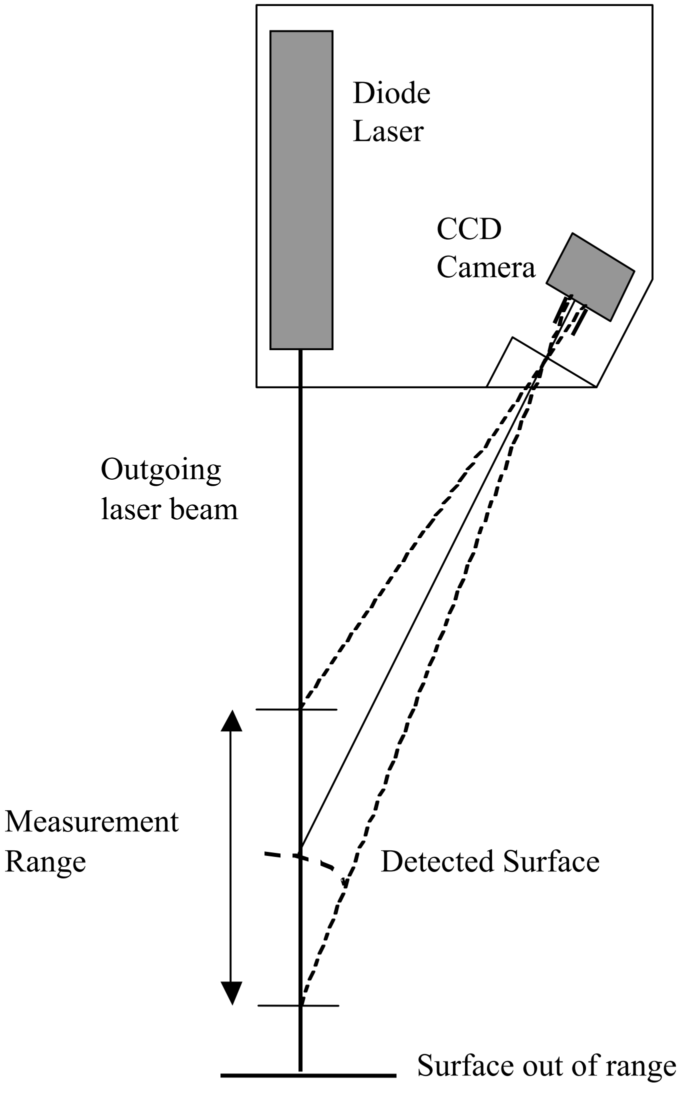

Figure 15. The Concentrator optical mapping facility uses optical micrometers which operate by detecting the diffuse reflection off a surface. Several different micrometers with different measurement ranges were used to select the grids and surfaces of interest on each pass of the mapping facility's translation stages.

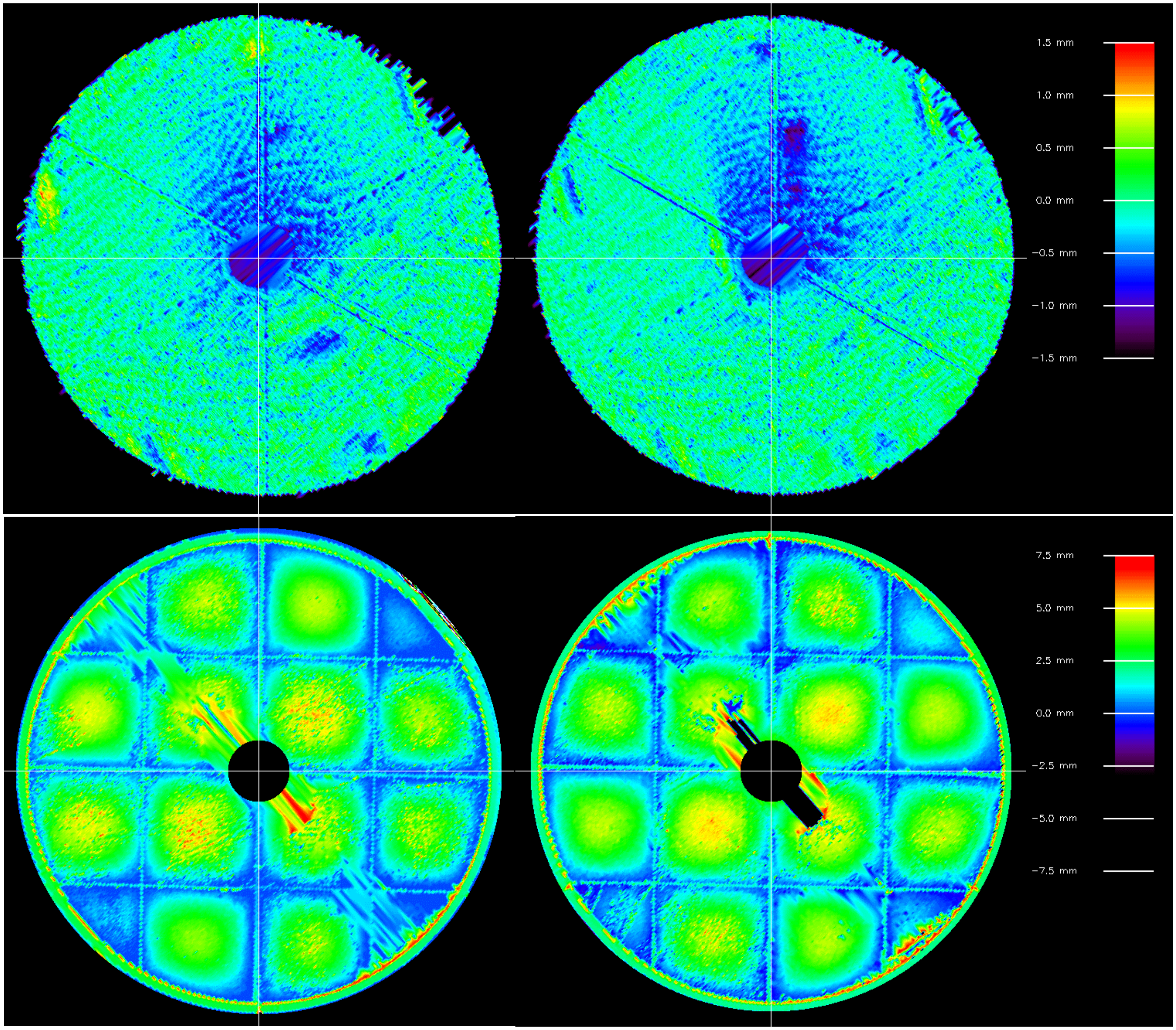

Before After

Figure 16. Color coded mapping of deviations from ideal for the FM acceleration grid surface (top) and FM domed grid (bottom) before and after vibration. The hydrogen rejection maps are referenced to a flat plane, while the domed grid maps are referenced to a paraboloid, so the dimples between supports are clearly visible. Only very small changes are visible indicating good dimensional stability for the grids.

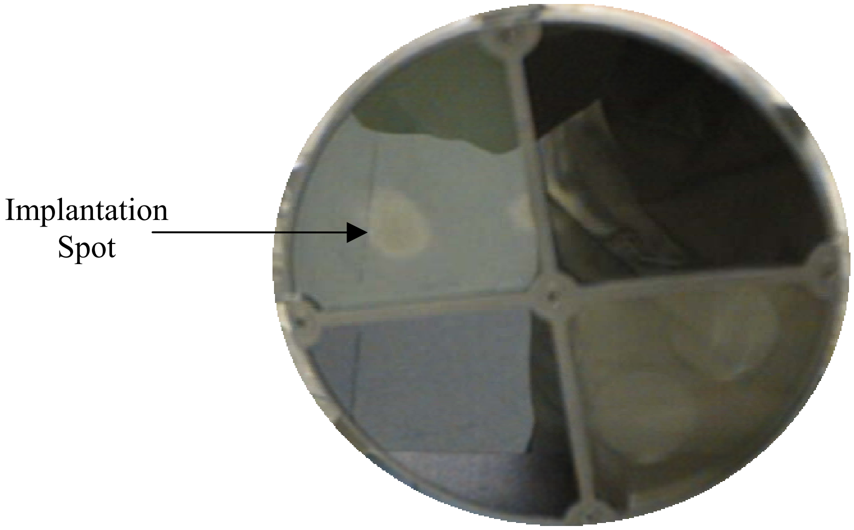

Figure 17. Concentrator target used for implantation test. The location of the implantation is clearly visible in a SiC segment. Several reflections from items on nearby work benches are also visible.

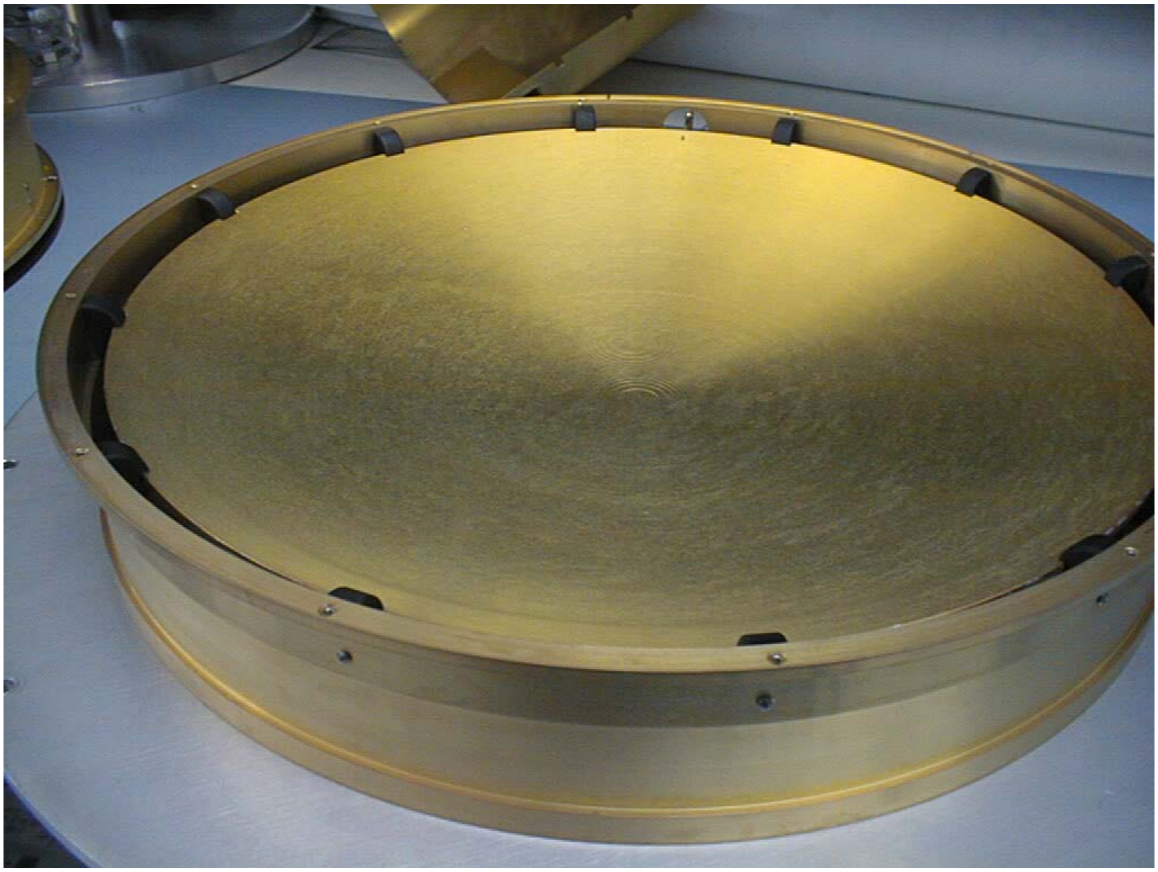

Figure 18. The lower portion of the Concentrator showing the microstepped mirror electrode. The N-doped SiC coated alumina insulators used around the edge of the mirror electrode appear black instead of the normal white of uncoated alumina. The opening in the housing and input post where the high voltage connection is made to the mirror electrode is also visible at the top of the photo.

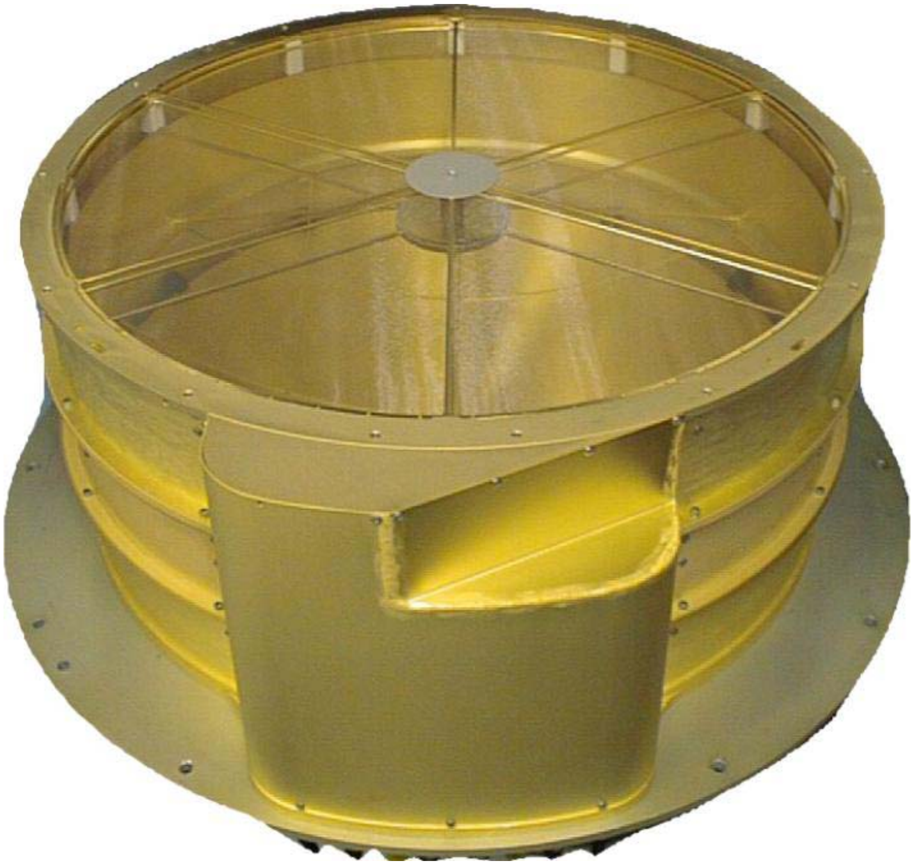

Figure 19. Final view of the FM Concentrator after gold coating, high voltage testing, and mapping in preparation for final mating with the science canister and spacecraft. The welded cover of the high voltage input section is closest to the camera.